Chair of Functional Materials and Materials Systems

Master's Thesis

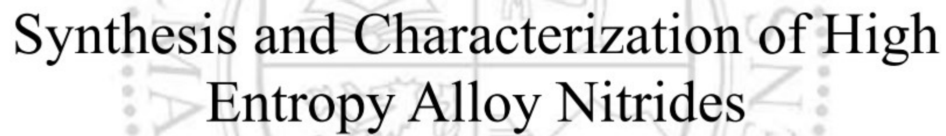

Synthesis and Characterization of High Entropy Alloy Nitrides

Michael Timo Tabelander, BSc

August 2023

2er, 3er, Fetzen … wurscht

– Michael Tabelander

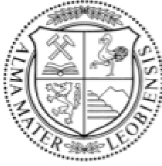

MONTANUNIVERSITÄT LEOBEN
www.unileoben.ac.at

EIDESSTATTLICHE ERKLÄRUNG

Ich erkläre an Eides statt, dass ich diese Arbeit selbständig verfasst, andere als die angegebenen Quellen und Hilfsmittel nicht benutzt, und mich auch sonst keiner unerlaubten Hilfsmittel bedient habe.

Ich erkläre, dass ich die Richtlinien des Senats der Montanuniversität Leoben zu "Gute wissenschaftliche Praxis" gelesen, verstanden und befolgt habe.

Weiters erkläre ich, dass die elektronische und gedruckte Version der eingereichten wissenschaftlichen Abschlussarbeit formal und inhaltlich identisch sind.

Datum 13.08.2023

Unterschrift Verfasser/in
Michael Timo Tabelander

Acknowledgments

I gratefully acknowledge the financial support from the Austrian Research Promotion Agency (FFG) (project number: 871687, PowerHEA).

I extend my sincere gratitude to Dr.mont. Univ.-Prof. Dipl.-Ing. Christian Mitterer, leader of the Chair of Functional Materials and Materials Systems at the Department of Materials Science, for his invaluable guidance and the opportunity to pursue this thesis.

Deep appreciation goes to Dr. Robert Franz and Dr.mont. Dipl.Ing. Georg Gruber for their mentorship, invaluable feedback, and corrections that greatly enriched my thesis.

Special thanks go to the entire thin-film group, particularly Sabrina Hirn and Magdalena Kirchmair, for their unwavering support and collaboration throughout my studies.

I am also thankful to my parents Rudolf and Christine Tabelander for granting me the chance to study at Montanuniversität Leoben and their constant encouragement and unwavering support. I would like to express my gratitude to my sibling, Alexander Tabelander, for both providing corrections and offering invaluable emotional support.

A heartfelt appreciation goes out to all the friends I connected with during my studies in Leoben, who have played a significant role in making this time so memorable. A special shoutout is reserved for Sebastian Stock, Fabian Stücklberger, Thomas Resch, Stefan Zeiler, Fabian Kadisch, Yves Godai, Elisabeth Grossfurtner, Daniel Nistelberger, Stefan Mutschlechner, Daniel Gass and Lukas Schretter.

I must express that this thesis would not have been possible without the contributions of these remarkable individuals, and I am truly appreciative of their support and guidance.

Content

Content V

1. Introduction 1
2. Theoretical background 3
   2.1. Magnetron sputtering 3
   2.2. High entropy alloys 10
   2.3. Residual stress 14
3. Experimental methods 17
   3.1. Film deposition 17
   3.2. Film characterization 18
4. Results and discussion 22
   4.1. Deposition 22
   4.2. Film characterization 25
   4.3. Thermal stability 33
5. Conclusions 44
6. References 45
7. Appendix 53

1. Introduction

Advancements in theoretical research on new materials and the advancement of relevant technologies have enabled the creation of metallic alloys containing more than three primary elements known as high-entropy alloys (HEAs). These HEAs, rooted in the concept of multi-principal elements, represent an innovative category of materials with extraordinary physical, mechanical, and chemical properties, making them highly promising for a wide array of applications [1]. Diverging from conventional alloys that heavily rely on just one or two major elements, with minor alloying elements added for enhancement, HEAs adopt a distinct and pioneering design approach. By incorporating at least five elements, each contributing atomic percentages between 5 and 35 at.%, This stability is achieved through the high entropy of mixing of the components (S_{mix} > 1.61 R, where R = 8.314 J mol^{-1} K^{-1} is the universal gas constant) HEAs free themselves from the constraints imposed by traditional designs. This newfound flexibility in alloy formulation allows for the precise tailoring of microstructures and properties [1].

The idea of these multicomponent alloys, sometimes referred to as multicomponent alloys, was first introduced by Yeh and Cantor during the early 2000s [2,3]. Yeh aptly coined the term "high entropy alloys" due to their characteristic high entropy of mixing. This high entropy phenomenon effectively obstructs the formation of intermetallic phases, thereby favoring the emergence of simpler cubic or hexagonal solid solution phases instead [1]. The distinctiveness of HEAs and their remarkable properties make them a compelling and captivating area of research in materials science and engineering.

Researchers have been enhancing the exceptional properties of HEAs, such as high hardness and strength, by incorporating nitrogen to form high entropy metal nitrides (HENs) [4]. This results in a NaCl-type fcc crystal structure, with N atoms occupying lattice voids and surrounding the metal atoms [4]. Ongoing research indicates a significant boost in hardness and elastic modulus as the N-content in the film increases. The enhanced hardness is attributed to the strong covalent bond between nitrogen and metallic elements, along with a higher degree of lattice distortion [4].

This thesis explores HEA and HEN thin films based on MoNbTaW and (MoNbTaW)N for a potential use as diffusion barriers in high power electronics, due to high melting point of the individual elements. These films are alloyed with a fifth element, specifically

Ti, V, Cr, Mn, Zr, or Hf. The deposition of all films was carried out using high power impulse magnetron sputtering (HiPIMS). Initially, the chemical composition, microstructure, mechanical and physical properties of the as-deposited MoNbTaW-based films were thoroughly examined. This investigation involved various techniques such as confocal 3D laser-scanning microscopy, energy-dispersive X-ray spectroscopy (EDX), transmission electron microscopy (TEM), X-ray diffraction (XRD), residual stress measurements, and resistivity measurements.

To evaluate the thermal stability of the films, annealing was performed in a vacuum furnace at temperatures of 500 °C, 700 °C, and 900 °C. After each annealing step, the same properties were reevaluated. Furthermore, in-situ stress measurements were conducted upon 810 °C to gain additional insights into the residual stresses of the films.

The thesis structure is as follows. Following the introduction, Chapter 2 provides a concise review of the PVD process, with particular emphasis on HiPIMS, HEAs, and an overview about residual stresses in thin films. This chapter also covers fundamental aspects of thin film growth. In Chapter 3, a comprehensive description of the experimental setup, deposition procedure, and characterization techniques is presented. The findings are then showcased and analyzed in Chapter 4. Lastly, Chapter 5 offers a summary of the main discoveries from this study and outlines potential directions for future research.

2. Theoretical background

2.1. Magnetron sputtering

Physical vapor deposition (PVD) methods are used to deposit films from a solid or liquid source. The vaporized material transfers to the substrate surface and the inner walls of the vacuum chamber where it condensates [5].

In case of sputter deposition, the target acts as the material source and cathode. The chamber walls and the substrate (mounted opposite of the target) act as the anode. During the process (Figure 2-1), a working gas is fed into the chamber and a negative potential is applied to the target. For the working gas, argon is typically used, as it is a noble gas with a comparatively large mass and rather low cost, compared to other noble gases (Ne: 0.9 g/dm³, 50 $/m³; Ar: 1.8 g/dm³, 68 $/m³; Kr: 3.7 g/dm³, 200 $/m³ [6]). The positively charged ions are mostly produced by impact ionization, which occurs when an electron knocks another one out of its atomic shell and the resulting ion is then accelerated towards the target [7].

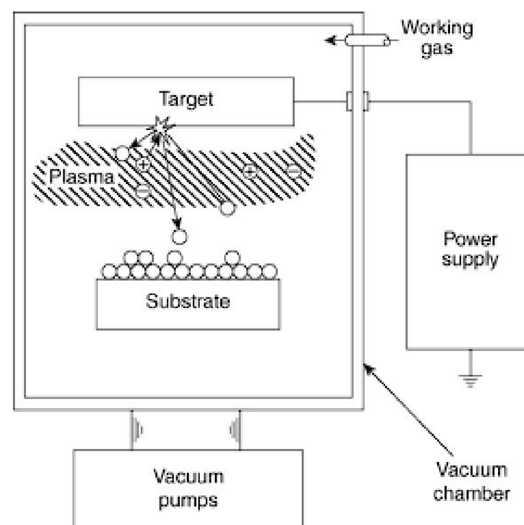

Figure 2-1: The basic sputtering process [8].

The ions kinetic energy is primarily lost as heat after colliding with the target surface, and to a smaller amount, it is transmitted to the target atoms, which may be ejected. Since the ejected atoms are mostly neutral, they are unaffected by the electric field. Secondary electrons are also emitted from the target surface as a result of the ion bombardment. These secondary electrons further ionize the working gas [8].

The secondary electrons emitted from the target surface are trapped in the field due to the Lorentz force:

$$\bar{F} = q(\bar{E} + \bar{v} \times \bar{B}) , \qquad (3.1)$$

where $\bar{F}$ is the Lorentz force acting on a particle with an electric charge q moving with a velocity $\bar{v}$ in an electric and magnetic field $\bar{E}$ and $\bar{B}$. Therefore, the electrons are forced to move in a cycloidal orbit parallel to the target and normal to the electric and magnetic field, resulting in a higher plasma density and increased ionization. Due to the higher ionization, an increased ion bombardment can be noticed, which results in higher sputtering and therefore deposition rates [8]. The plasma hovers in a torus-shape above the target leading to a non-uniform erosion pattern, resulting in a reduced (~26 – 45 %) target usage [9]. Magnetron sputtering can be further differentiated in conventional magnetron sputtering and unbalanced magnetron sputtering, shown in Figure 2-2. While all magnetic field lines are closed by the opposite pole of the other magnet in the conventional mode, within the unbalanced mode a part of the magnetic field lines is not closed. The plasma in conventional magnetron mode is tightly contained close the target surface. Thus, the substrate is positioned outside of this area and will not be bombarded with ions. In unbalanced mode, the magnetic field lines are directed to the chamber (Type-1) or to the substrate (Type-2), depending on the relation of strength between the central and outer magnetic pole. The advantage of the Type-2 configuration is that it also increases the ion and electron density close to the substrate. As a result, higher quality films can be deposited [10].

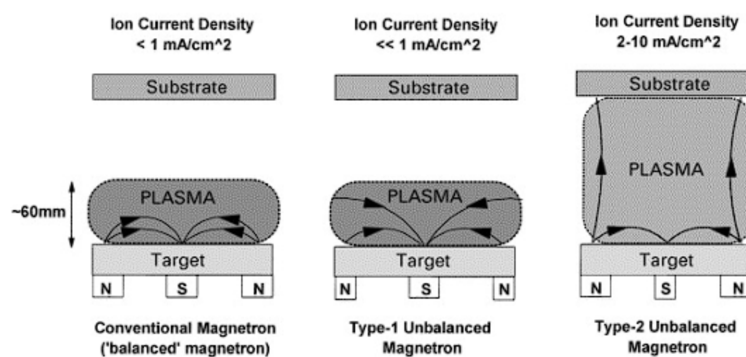

Figure 2-2: Schematic illustration of the plasma in conventional and unbalanced magnetrons [10].

2.1.1. High power impulse magnetron sputtering

During high power impulse magnetron sputtering (HiPIMS), short electrical impulses are applied to the target. This results in a much denser plasma and a higher sputtered material ionization of up to ~70 %, compared to ~1 % in conventional magnetron

sputtering [8,11]. The ions bombarding the target surface in HiPMS can be separated into three different groups: primary ions of the working gas, recycled ions of the working gas, and ions of the target material, shown in Figure 2-3. Which types of ions are primarily present, depends on the target material, the pulse length, or the applied power and results in a large variation of current waveforms in HiPIMS pulses [12,13].

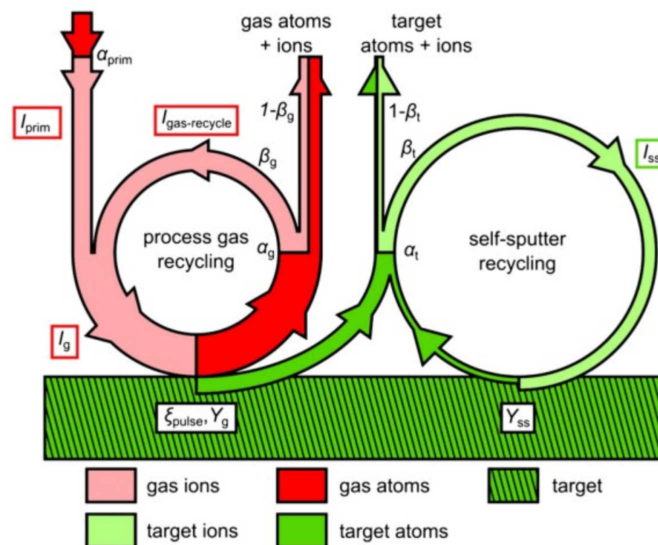

Figure 2-3: Schematic of the combined processes of process gas recycling and self-sputter recycling [12].

Therefore, HiPIMS can be categorized according to the current pulses of the HiPIMS discharge into the five different discharge modes shown in Figure 2-4, depending on the occurring ions [13]:

- **Working gas sputtering:** This process involves primarily the use of working gas ions, without any recycling of either the working gas or target ions (two bottom curves of Figure 2-4).
- **Working gas sustained self-sputtering:** The ionization of the working gas is necessary in order to sputter enough target atoms, which will then be ionized and drawn back to the target, initiating a cycle of recycling of the target atoms (middle curve of Figure 2-4).
- **Self-sustained self-sputtering:** The sputtered species undergo significant ionization, with a large portion of the ions being drawn back to the target to sputter more target atoms, which are then ionized as well. This process of target atom recycling allows the discharge to be sustained solely through the sputtered species, meaning that it can operate without the use of a working gas (two top curves of Figure 2-4).

- **Self-sputter runaway:** The self-sputtering process is amplified due to a positive feedback loop, in which the self-sputter parameter surpasses unity and causes the self-sputtering to accelerate or become uncontrolled.
- **Working gas recycling:** During the pulse, some of the neutralized working gas ions return to the discharge and become ionized again. This initiates a series of gas recycling as these newly ionized gas particles are drawn back to the target (two top curves of Figure 2-4).

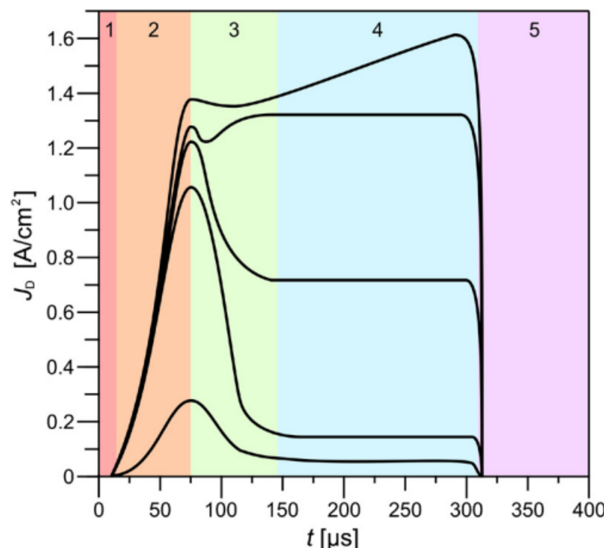

Figure 2-4: Different HiPIMS discharge waveforms. The current discharge can be separated into five phases: (1) ignition, (2) current rise to first maximum, (3) transition phase, (4) plateau/runaway, and (5) afterglow [14].

In comparison to conventional magnetron sputtering, high-quality thin films with superior adhesion, denser structure, higher hardness, and a smoother morphology can be obtained, due to high ionization rate of the sputtered species [15]. A disadvantage of HiPIMS is the lower deposition rate compared to direct current magnetron sputtering. One explanation for the decreased deposition rate during HiPIMS is the back attraction of a certain fraction of the ionized part of the sputtered atoms [11,15].

2.1.2. Reactive magnetron sputtering

Reactive magnetron sputtering is applicable to deposit non-metal thin films by using a reactive gas, which is mixed with the inert working gas and then reacts with the sputtered metal atoms [16]. Commonly used reactive gases are N_2, O_2, CH_4, etc. to produce nitride, oxide, oxynitride or carbide films [7].

In general chemisorption of the reactive gas on the surface of the substrates takes place and can be characterized by the sticking coefficient S, which depends on the materials used for the chamber wall, the substrate and the target surface [17]. Another

mechanism observable is the direct implementation of reactive gas ions. The combination of both mechanisms is referred as ion impact enhanced chemisorption and was reported to take place in HiPMS mode [17]. The reaction always takes place on the substrate, the surface of the target or the walls of the chamber, where the energy of production may be easily dissipated without breaking down the newly created compound. Complex molecules tend to break down spontaneously in the gas phase, because the atoms and products have too much kinetic energy and cannot disperse it [17].

One important aspect of reactive sputtering is the formation of a hysteresis, which can be observed in the deposition rate, discharge voltage and the partial pressure of the reactive gas. Thus, three main regions of operation can be defined dependent on the reactive gas flow, shown in Figure 2-5 [18]. A metal mode is maintained with a high rate of substoichiometric compound deposition for low reactive gas flows. The sputter process is not considerably impacted by the addition of the reactive gas, since all the provided reactive gas is completely incorporated in the film. As the flow of the reactive gas rises, the mass of the gas atoms contributes to the mass of the deposited metal, increasing the mass deposition rate considerably [18,19]. The deposition rate rapidly decreases when the reactive gas flow increase triggers the change to the compound mode (point A – B in Figure 2-5). All the sputtered metal is transformed into compound material at this rate of reactive gas flow, and the reactive gas reacts with the surface of the target. Further increasing the reactive gas flow has no impact on the mass deposition rate. After decreasing the gas flow again, the compound mode is still present up to point C, when another rapid transition to metal mode can be observed (point C – D in Figure 2-5). When depositing in transition region (A – B – C – D in Figure 2-5), it is possible to tune the film stoichiometry and the deposition rate, depending on the process history [18,19].

The first transition from metal into compound mode (point A – B in Figure 2-5) can be explained by reduction of the fraction of sputtered metal surface on the target in comparison to the formed compound fraction. This results in a reduced consumption of reactive gas. The second transition (point C – D in Figure 2-5) can be observed, when the reactive gas flow is getting reduced so that not enough reactive gas is available to form the compound. Consequently, much more metal is deposited, and the systems shifts to the metal mode again [18].

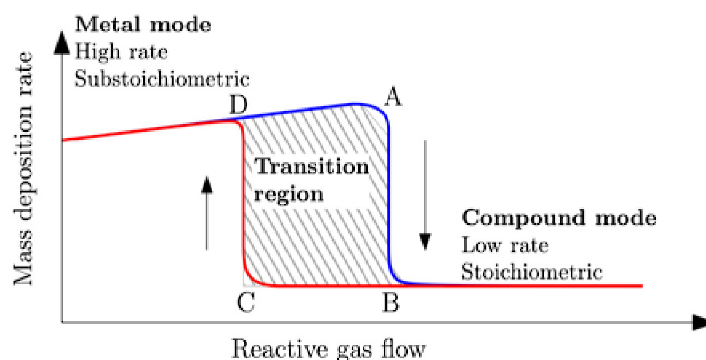

Figure 2-5: Deposition rate evolution with reactive gas flow. Pronounced hysteresis (wide transition region) defined by the transitions A–B and C–D is shown [18].

Several investigations have shown that using HiPIMS reduces hysteresis in reactive sputtering. From a technical perspective, the potential of a high deposition rate of a stoichiometric compound in the transition mode or near to the transition from metal mode is the most significant result of hysteresis-free operation utilizing HiPIMS [18].

2.1.3. Thin film growth and structure zone models

When vaporized atoms reach the substrate, they can either be quickly reflected or absorbed as adatoms on the surface. Adatoms spread throughout the surface of the substrate before either re-evaporating or interacting with one another to create metastable clusters. Once they reach a threshold size, these clusters also known as nuclei, become thermodynamically stable. Afterwards the growth stage follows, during which the nuclei expand either as a result of adatoms diffusing over the surface or as a direct result of the incident species impinging on them [8,20]. The formation steps of a polycrystalline film are shown in Figure 2-6.

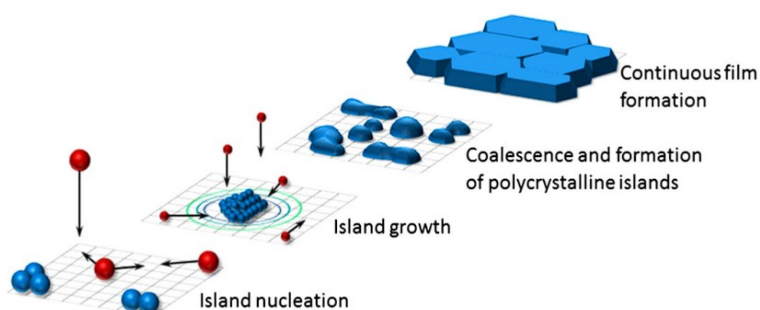

Figure 2-6: Schematic illustration of thin film formation stages [20].

In general, three growth modes of thin films can be differentiated (Figure 2-7): Volmer-Weber growth which is also called island-growth, Stranski-Krastanov growth, or Frank-van der Merwe growth which is also called layer-growth. The adsorbate-adsorbate interactions in the Volmer-Weber growth are stronger than the adsorbate-surface

interactions. Therefore, three-dimensional islands of adatoms are formed and consequently grow together as they increase in size. In the Stranski-Krastanow growth, the opposite can be observed, as the adsorption energy is larger than the bonding energy of the adatoms. Thus, joints-islands or layer-islands are formed. Adsorbate-surface and adsorbate-adsorbate interactions are balanced in the Frank-van der Merwe growth mode, which is also known as layer-by-layer growth. Given that it needs perfect lattice matching between the thin film and its substrate, the Frank-van der Merwe growth model is frequently restricted to homoepitaxy. The depositing atoms are equally attracted to the substrate and the already condensed adatoms for Frank-van der Merwe growth to take place [21,22].

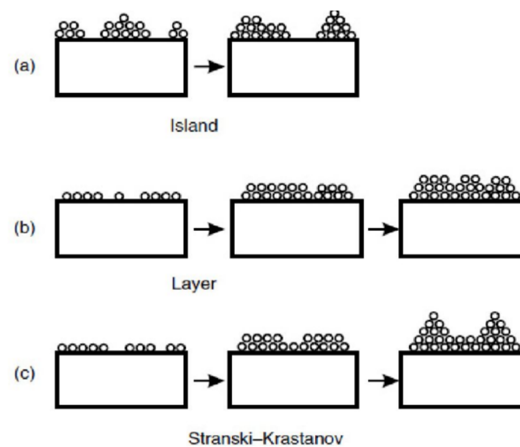

Figure 2-7: Modes of growth of film: (a) Volmer–Weber growth, (b) Frank-van der Merwe layer growth, and (c) Stranski-Krastanov layer plus island growth [23].

The properties and microstructure of thin films are highly dependent on the deposition parameters, leading to a wide range of characteristics and properties. To summarize the influence of deposition parameters on microstructure or morphology, structure zone models (SZM) were developed. The first SZM was introduced by Movchan and Demchishin [24], who connected the microstructure to the homologous temperature T_s/T_m, where T_s is the substrate temperature and T_m is the melting temperature of the deposition material [24]. By incorporating the working gas pressure dependence, Thornton modified this SZM for sputter-deposited films, which was later replaced with the bias voltage by Messier et al. [25,26]. The most recent SZM was proposed by Anders [27] (Figure 2-8) and incorporates a generalized temperature, T^*, a normalized energy flux, E^*, as parameters, resulting in net film thickness t^*. T^* includes the homologous temperature as well as the potential energy of the arriving ions. The energy flux E^* can be described as displacements and heating effects caused by the kinetic energy of bombarding particles [27].

This SZM is defined by four zones which describe the formed film morphology. Zone 1 is characterized by a high nucleation density, due to a low surface mobility of adatoms. This results in a fine-grained, fibrous-like structure with a high density of lattice imperfections, such as voids [7]. In the second zone, also called transition zone T, crystal growth is the dominant structure forming phenomena in the growth of V-shaped grains. In comparison to zone 1, surface diffusion of adatoms can be observed but is still limited [26]. Zone 2 is mainly driven by grain growth, due to surface diffusion. Films deposited in this zone show a columnar structure with dense grain boundaries. In zone 3, also bulk diffusion occurs, which causes recrystallization, grain coarsening, and densification, which has a significant impact on the film formation. The film morphology shows large equiaxed grains [7].

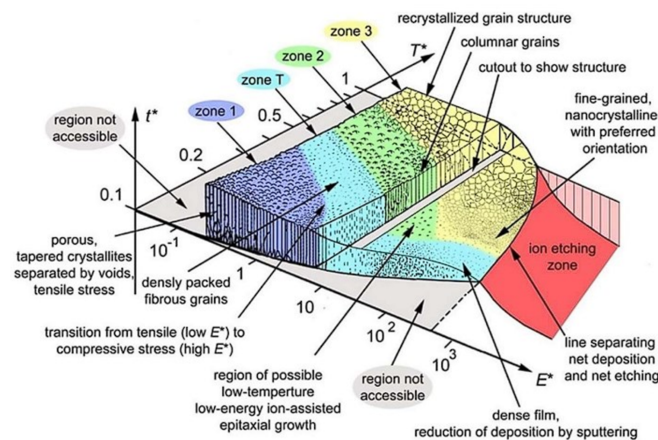

Figure 2-8: Structure zone model for depositing thin films and coatings as proposed by Anders [27].

2.2. High entropy alloys

2.2.1. Definition

High-entropy alloys (HEAs) are often defined by the mixing entropy and consist of at least 5 elements, with a concentration between 5 and 35 at.% [28,29]. The mixing entropy consists of four contributions: configurational, vibrational, magnetic dipole, and electronic randomness, whereas the configurational entropy is dominant and is often used as the mixing entropy [1]. The configurational entropy per mole of an n-component solid solution with X_i as the mole fraction of the ith component equals:

$$\Delta S_{conf} = -R \sum_{i=1}^{n} X_i \ln X_i \,, \tag{3.2}$$

where R is the gas constant. The configurational entropy achieves its maximum for an equimolar alloy. With increasing number of elements in equimolar and non-equimolar

ratios, the configurational entropy grows. E.g., for a 5-element based alloy, with all elements in equimolar composition, the calculated configurational entropy equals $\Delta S_{conf} = 1.61\,JK^{-1}$ [1].

High entropy effect

The stability of phases increases with the decrease of the Gibbs free energy of mixing ΔG_{mix} and can be calculated using:

$$\Delta \mathrm{G_{mix}} = \Delta H_{mix} - T\Delta S_{mix}, \tag{3.3}$$

where ΔH_{mix} describes the mixing enthalpy, T the temperature and ΔS_{mix} the mixing entropy [30]. When ΔS_{mix} increases, $\Delta \mathrm{G_{mix}}$ decreases, therefore HEAs often consist mainly of simple bcc, fcc or hexagonal solid solution phases, instead to intermetallic compounds. This is called the high entropy effect, which is one of the core effects of HEAs. The other core effects are the sluggish diffusion effect, the severe lattice distortion effect, and the cocktail effect, which are described in the following paragraphs [1].

Severe lattice distortion effect

The severe lattice distortion can be explained by the fact, that HEAs consist of elements with different atomic radii occupying one single extremely distorted lattice in the crystal structure. For sufficiently significant atomic size differences, the deformed lattice will collapse into an amorphous structure as the lattice distortion energy would be too high to be maintained [31]. The lattice distortion effect , whether in crystalline or amorphous arrangements, impacts the alloy's mechanical, thermal, electrical, optical, and chemical characteristics. For instance, high solid solution hardening, high thermal and electrical resistivity [28] are directly linked to the lattice distortion effect.

Sluggish diffusion effect

The sluggish diffusion effect is theorized and states that a combination of atomic sizes will result in more pronounced diffusion barriers and slower diffusion than in other alloys or compounds [32].

For instance, this will have an impact on the characteristics of corrosion and transport, but it will also cause kinetic factors during sample synthesis, favoring the creation of simple solid solution phases [32].

Cocktail effect

According to the composition and processing, HEAs may consists of one or more phases. Consequently, the interplay of factors such as grain shape, distribution of grain sizes, interfaces between grains and phases, and the attributes of each phase, collectively shape the properties exhibited by the individual phases. It's important to note that each phase essentially constitutes a solid solution, comprising numerous elemental components, resembling a composite on the atomic scale. The composite characteristics arise from the interplay among all constituents, coupled with substantial lattice distortion, alongside the inherent elemental properties dictated by the mixing rule [1,33].

2.2.2. Refractory High Entropy Alloys

Refractory High Entropy Alloys (RHEA) were first introduced by Senkov et al. [28] in 2010, who studied MoNbTaW and MoNbTaVW produced by vacuum melting. RHEAs are HEAs which are mainly containing refractory metals, i.e., Nb, Mo, Ta, W and Re. Additionally, RHEAs are frequently mixed with elements belonging to the broader category of refractory metals, such as Cr, Hf, Ti, V and Zr. Most of the synthesized RHEAs show a bcc structure, since metals of subgroups V and VI have a bcc lattice structure [34].

MoNbTaW based alloys have gained significant attention in recent years due to their unique combination of properties. One of the main areas of research for MoNbTaW based alloys are the mechanical properties, including strength, ductility, and toughness [35]. Researchers have found that by tuning the alloy's composition and processing conditions, they can achieve exceptional mechanical properties that rival or exceed those of traditional high-strength materials [35]. Another area of research for MoNbTaW based alloys are their good high-temperature properties, including thermal stability and oxidation resistance [35]. Due to their refractory nature, MoNbTaW based alloys are capable of maintaining the strength and structural integrity at high temperatures, making them a promising material for high-temperature applications such as turbine blades and exhaust components [34–36].

Magnetron sputtering is a commonly used approach for synthesizing HEAs. This method allows for the deposition of thin films by adjusting the process parameters and it is possible to manipulate the microstructure and properties of the deposited HEA films [1,28].

Numerous studies have examined the potential applications of MoNbTaW-based RHEA thin films. In one such study, it was found that the hardness of nanocrystalline MoNbTaW films increased with longer annealing times at 800 °C in vacuum due to the formation of amorphous intergranular films [37]. Similarly, MoNbTaVW films, deposited using cathodic arc deposition (CAD), displayed an increase in hardness up to 1000 °C, but a decrease in hardness at temperatures up to 1300 °C. These films remained stable up to at least 1500 °C, making them ideal for high-temperature applications [38]. The properties of MoNbTaVW films were compared for different deposition angles and methods, with all films displaying a solid solution bcc crystal structure irrespective of the deposition angle or method [39]. The potential use of MoNbTaVW films for interconnects of solid oxide fuel cells and coatings for thermoelectric elements was investigated, and the influence of varying V content on the hardness and Young's modulus of the films was also studied [40,41]. Recent studies by Gruber et al. [42] also suggest a possible application as diffusion barriers in microelectronics, due to their good thermal stability.

Overall, the state-of-the-art research on MoNbTaW based alloys is focused on developing a fundamental understanding of their structure-property relationships and exploring their potential for a wide range of applications in the aerospace, energy, microelectronic and automotive industries [35,36].

2.2.3. High entropy metal nitrides

To further improve the excellent properties of HEAs, e.g., high hardness and high strength, researchers tried to incorporate nitrogen to form high entropy metal nitrides (HEN) [43]. The N atoms usually occupy lattice voids and form a NaCl-type fcc crystal structure, where the metal atoms are surrounded by N [4].

Ongoing research on HEN showed a significant increase in hardness and elastic modulus with increasing N-content in the film. The increased hardness can be explained as a result of the strong covalent bond between nitrogen and metallic elements. Further, the addition of nitrogen results in a higher degree of lattice distortion, which also leads to a strengthening effect [43,44]. Other research on (AlCrTiVZr)N films by Xu et al. [45] reported a decrease in wear rate with increasing N-content, which leads to a possible application as protective films.

In RHEAs nitrides, based on MoNbTaVW and studied by Xia et al. [46], The addition of nitrogen markedly impacts the chemical makeup, structure, as well as the electrical

and mechanical traits of (MoNbTaVW)N films synthesized by CAD and direct current magnetron sputtering (DCMS). The metal ratio in the films remained constant despite the varying N content, reflecting the composition of the target. Only one phase at a time was detected in the films through XRD analysis and increasing N content led to a shift from a bcc to a fcc phase, occurring at a N concentration of 25 to 30 at.%. This transition was minimally influenced by film growth conditions and was primarily dictated by the metal to N ratio. Incorporating N also increased film hardness, reaching up to 30 GPa, typical of fcc transition metal nitride phases, but adversely affected electro-mechanical properties as the fcc nitride phase exhibited a lower crack onset strain, resulting in an earlier failure in tensile tests [46].

Another possible application for HEN and refractory HEN might be the use as diffusion barriers, which was already reported for (AlCrTaTiZr)N [47], (AlCrTaTiZrMo)N [48] and (TiVCrZrHf)N [49]. All studies concluded that inter-diffusion between Cu and Si was successfully suppressed.

2.3. Residual stress

2.3.1. Residual stress of thin films

Generally, film stresses can be divided into three categories, intrinsic stresses, extrinsic stresses, and thermal stresses [50]. Intrinsic stresses are created during the growth of the film and strongly depend on the material, the substrate, the substrate temperature, the growth flux, the damage caused by the impinging ions and chamber conditions. Due to different lattice structures of substrate and film, residual stresses and lattice defects may arise during deposition. Extrinsic stresses emerge from changes in the physical environment. The mismatch between the thin film's and the substrate's coefficients of thermal expansion (CTE) causes residual stresses during cool down from the deposition temperature to room temperature. These stresses are also called thermal stresses [50].

2.3.2. Residual stress measurement with wafer curvature

A convenient way to measure stress within thin films is the wafer curvature method. Depending on the deposition conditions, there can be a large initial stress present in the as deposited film. The stresses are leading to a curvature of the sample and can be measured, if the film or the back of the substrate is reflective, using laser-beams and photodiodes. Further limitations concerning the sample geometry can be found in

[51]. The average residual stress in the film can be calculated by the modified Stoney equation [52]:

$$\sigma_f = M_S \frac{d^2}{6\,t\,R} \tag{3.4}$$

There, σ_f is the mean stress in the film, d and t the thickness of the substrate and film, R the radius of curvature and M_s the biaxial modulus of the substrate. The curvature of the substrate itself must be measured and deducted from the curvature of the film substrate compound at the appropriate temperature if the absolute stress should be measured [53,54].

With additional heating, the thermo-mechanical behavior of thin-films can be studied. A typical stress-temperature curve of a Mo-Ag thin film on Si is shown in Figure 2-9 [55]. The measurement starts at room temperature at the thermo-cycle point (I) until reaching point (II). In between point (I) and (II) only elastic deformation takes place and the slope can be calculated with:

$$\frac{d\sigma}{dT} = \Delta\alpha \frac{E}{1-\nu}, \tag{3.5}$$

where $\Delta\alpha$ describes the difference of the CTE between substrate and film, E the Young's modulus and ν the Poisson's ratio of the film [55].

Further heating leads to non-elastic deformation, due to mechanisms such as grain growth or dislocation gliding and general healing of defects. When reaching point (III) shown in Figure 2-9, a plateau can be observed, due to the compensation of the material compaction with creep strain and thermo-elastic strain. Afterwards, the stress rises because of grain growth, diffusion, or changes in the dislocation structure. Cooling starts at point (V) shown in Figure 2-9 and a thermo-elastic line is found. Further cooling increases the stress, while decreases the creep-velocity [55,56].

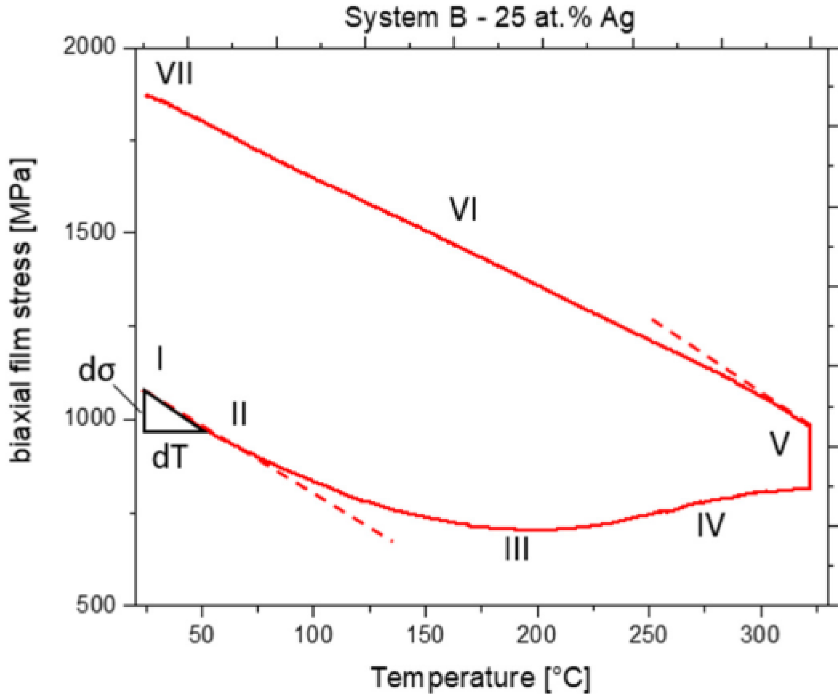

Figure 2-9: Thermal evolution of stress of a Mo-Ag thin film on Si [57].

3. Experimental methods

3.1. Film deposition

The films were deposited on polished B-doped (100) Si substrates (7 mm x 21 mm x 0.3 mm). The used 10 substrates were ultrasonically cleaned in an acetone bath for 7 min and then in an ethanol bath for the same amount of time. After cleaning, a blow dryer was used to dry the substrates before mounting them on a substrate holder. A lab-scale deposition system was used to deposit the films. For the deposition of the films, equimolar MoNbTaTiW, MoNbTaVW, CrMoNbTaW, MnMoNbTaW, MoNbTaWZr and HfMoNbTaW targets with a diameter of 76 mm were used. The targets were produced by Plansee Composite Materials GmbH. The pumping system of the deposition facility consists of two pumps working in tandem. A rotary vane pump (Pfeiffer Vacuum Duo 20) first evacuates the chamber to a base pressure of around 90 Pa prior to deposition. Afterwards the chamber is further evacuated to roughly 10^{-4} Pa using a turbomolecular pump (Pfeiffer Vacuum HiPace 700). Ar and additional N_2, when depositing nitrides, were employed as working/reactive gases. The flow rates of Ar and N_2 were changed using a Brooks Instrument thermal mass flow controller. During film deposition, a Baratron capacitance manometer (MKS Instruments) detects the gas pressure within the chamber. The Ar flow and N_2 flow were set in standard cubic centimeter per minute (sccm) according to the deposition parameters shown in Table 1, which leads to a working gas pressure of 3 Pa or 2.5 Pa, respectively. A working pressure of 2.5 Pa was used for the metal MnMoNbTaW film, due to delamination of the film deposited at 3 Pa. The deposition chamber was equipped with an unbalanced magnetron sputtering source. The magnetron sputtering source was powered by an ADL GmbH DC power supply (type GS 30/1000) linked to a MELEC GmbH SPIK3000A-10 pulse power generator. With an average power of 400 W and a frequency of 100 Hz, the deposition was performed in HiPIMS mode. Furthermore, the current and voltage peak were recorded with an oscilloscope. The substrates were only heated by the plasma in the chamber, as no additional heating was applied to the substrate. Furthermore, the substrates were grounded and no bias voltage was applied. The temperature was measured with a thermo-couple nearby the samples and reached a maximum temperature of 90 °C within the first few minutes of the deposition. Following each deposition run, the chamber was vented with N_2 to atmospheric pressure.

Table 1: Deposition parameter and sample IDs used in the present work.

Sample ID	Target	Deposition time [min]	Working pressure [Pa]	Ar-flow [sccm]	N_2 flow [sccm]	N_2 partial pressure [Pa]
HEA_Ti_MT_01	MoNbTaTiW	90.0	3.0	190.0	0	0
HEA_Ti-N_MT_08	MoNbTaTiW	90.0	3.0	187.2	2.8	0.09
HEA_Ti-N_MT_09	MoNbTaTiW	90.0	3.0	178.0	12.0	0.36
HEA_Ti-N_MT_12	MoNbTaTiW	4.5	3.0	187.2	2.8	0.09
HEA_Ti-N_MT_13	MoNbTaTiW	4.5	3.0	178.0	12.0	0.36
HEA_V_MT_01	MoNbTaVW	90.0	3.0	190.0	0	0
HEA_V-N_MT_01	MoNbTaVW	90.0	3.0	187.2	2.8	0.09
HEA_V-N_MT_02	MoNbTaVW	90.0	3.0	178.0	12.0	0.36
HEA_Cr_MT_03	CrMoNbTaW	90.0	3.0	190.0	0	0
HEA_Cr-N_MT_01	CrMoNbTaW	90.0	3.0	187.2	2.8	0.09
HEA_Cr-N_MT_02	CrMoNbTaW	90.0	3.0	178.0	12.0	0.36
HEA_Mn_MT_03	MnMoNbTaW	90.0	2.5	153.0	0	0
HEA_Mn-N_MT_01	MnMoNbTaW	90.0	3.0	187.2	2.8	0.09
HEA_Mn-N_MT_02	MnMoNbTaW	90.0	3.0	178.0	12.0	0.36
HEA_Zr_MT_02	MoNbTaWZr	90.0	3.0	190.0	0	0
HEA_Zr-N_MT_01	MoNbTaWZr	90.0	3.0	187.2	2.8	0.09
HEA_Zr-N_MT_02	MoNbTaWZr	90.0	3.0	178.0	12.0	0.36
HEA_Hf_MT_02	HfMoNbTaW	90.0	3.0	190.0	0	0
HEA_Hf-N_MT_01	HfMoNbTaW	90.0	3.0	187.2	2.8	0.09
HEA_Hf-N_MT_02	HfMoNbTaW	90.0	3.0	178.0	12.0	0.36

3.2. Film characterization

The film thickness was measured using a Keyence confocal 3D laser-scanning microscope (CLSM), VK-X1100 series, which was also used for surface images.

Transmission electron microscopy (TEM) was used for analyzing the morphology of two (MoNbTaTiW)N films, deposited for 4.5 min on TEM-grids, using a Joel 2100 F TEM. In addition, both films were examined with selected area electron diffraction (SAED).

The chemical composition of the films was determined by energy-dispersive X-ray spectroscopy (EDX) with a Bruker Type XFlash 6-60 detector, which is attached to a Tescan Magna scanning electron microscope (SEM).

X-ray diffraction (XRD) was used to examine the microstructure of the films using a Bruker-AXS D8 Advance diffractometer equipped with parallel beam optics and a Cu-K_α radiation source. All measurements were done in Bragg-Brentano geometry. With

a resolution of 0,02 ° and a step duration of 1 s, the films were scanned in the 2Θ diffraction angle range from 20 ° to 95 °.

A Jandel Model RM2 cylindrical four-point probe was used to measure the resistivity of the films. Five measurements were performed on each sample, two crosswise to the long side of the sample and three lengthwise to the sample. The resistance R_s of the films can be calculated according to [58]:

$$R_s = \frac{\pi}{\ln(2)}\left(\frac{\Delta V}{I}\right), \tag{4.1}$$

were ΔV describes the measured voltage and I the set current. Together with the thickness t, the resistivity ρ can be calculated [58]:

$$\rho = R_s t. \tag{4.2}$$

The laser-based wafer curvature measurement was used to detect the residual stress within the film at room temperature, the basic setup is shown in Figure 3-1. The sample surface first reflects two parallel laser beams with a set distance d, which are then reflected by a mirror at a height $h/2$. The curvature radius R of the sample can be calculated by measuring the separation d' between the beams that are reflected on the measuring plate:

$$R = \frac{2hd}{d'-d}. \tag{4.3}$$

With the help of the modified Stoney equation [52]

$$\sigma_f = M_S \frac{d^2}{6\,t\,R}, \tag{4.4}$$

the residual stress of the film can be calculated.

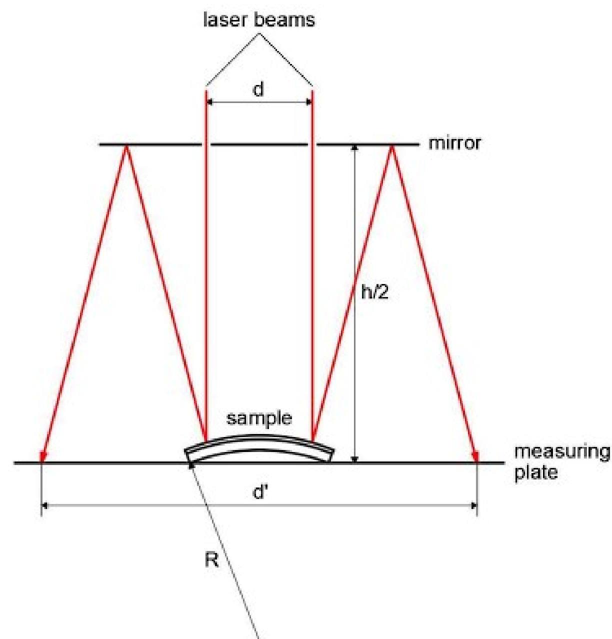

Figure 3-1: Illustration of a basic wafer curvature setup [59].

Also, the stress evaluation while annealing of the samples was measured using the wafer curvature method. There, a k-Space Associates multibeam optical sensor system (MOS) was used. A systematic drawing is shown in Figure 3-2. The measuring principle of both wafer curvature methods are the same, just different devices were used. The MOS works by passing a laser through several etalons, which produce a variety of spots that bounce off the substrate's surface and are photographed by a charge-coupled device (CCD) camera. The substrate bends in response to the mechanical stress as the film is heated or cooled (equation 3.5), with the radius of curvature depending on the amount of residual stresses within the film (equation 3.5). The positions of the reflected laser spots are altered by the substrate curvature. The stresses in the sample can as well be calculated using the modified Stoney equation. To study the thermomechanical behavior, all films were heated in vacuum from room temperature to 810 °C, cooled down to 80 °C, afterwards the heating and cooling cycle was repeated, with the difference that the samples were cooled down to room temperature in the end. Heating and cooling rates were kept constant at 9.6 K/min.

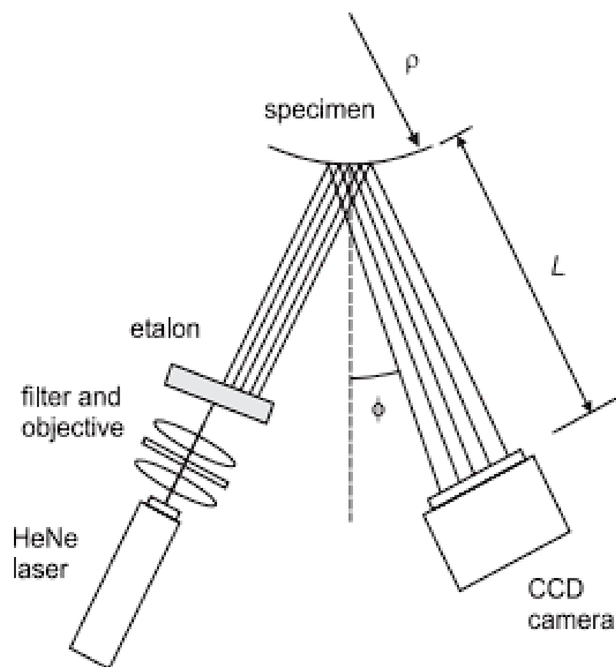

Figure 3-2: Schematic drawing of the curvature measurement [50].

In addition, the films were annealed in a HTM Retz vacuum furnace at around 10^{-6} Pa. Initially, the films were heated to 250 °C at a rate of 20 K/min and held at this temperature for 30 min. Then, the films were heated to the annealing temperature at a rate of 30 K/min, and held at a constant temperature for 15 min. Annealing was performed at 500 °C, 700 °C and 900 °C. The films were afterwards cooled down to room temperature.

4. Results and discussion

4.1. Deposition

4.1.1. Deposition parameter study

The first set of (MoNbTaTiW)N depositions were conducted at a pressure of 1 Pa, but all the films produced at this pressure delaminated immediately. Thus, the pressure was increased to 2 Pa, but this did not solve the issue and the films delaminated as well. Ultimately, a pressure of 3 Pa was found to produce films, which adhere to the substrate, since higher pressures result in lower compressive residual stresses [8]. However, there was one exception with the metal MnMoNbTaW film, which had to be deposited at a pressure of 2.5 Pa as it was not possible to synthesize it at 3 Pa without causing delamination. Excessively high pressures may lead to higher tensile stresses in the films [8], which in turn leads to cracking.

4.1.2. HiPMS discharge

The current and voltage pulses of the HiPIMS discharge of the MoNbTaTiW, CrMoNbTaW and MoNbTaWZr targets are shown in Figure 4-1. The discharge pulses of the other alloys can be found in the appendix. In general, the voltage pulse, generated by the power supply, shows a near rectangular shape and reaches a plateau after approximately 25 µs of the 100 µs pulse on-time. The current discharge curves vary depending on the target-material and nitrogen flow. However, in all cases, the current reaches a maximum after 50 µs to 75 µs and decreases to lower values afterwards. For most of the depositions (Figure 4-1 (b), (c), (d), (e), (f), (i)) the pulse on-time was too short to exactly determine which deposition mode is present, since the current cut-off occurs shortly after reaching the maximum. However, in case of the metal films of MoNbTaTiW and MoNbTaWZr (Figure 4-1 (a), (g)) as well as the (MoNbTaWZr)N film deposited at lower nitrogen partial pressure (Figure 4-1 (h)) it was found that working gas sustained self-sputtering is most likely to occur, when comparing the discharge pulses with the literature [5]. Thus, the ionization of the working gas is necessary in order to sputter enough target atoms, which will then be ionized and drawn back to the target, initiating a cycle of recycling of the target atoms [13]. Gruber et al. [60] already reported the occurrence of working gas sustained self-sputtering for similar deposition parameters.

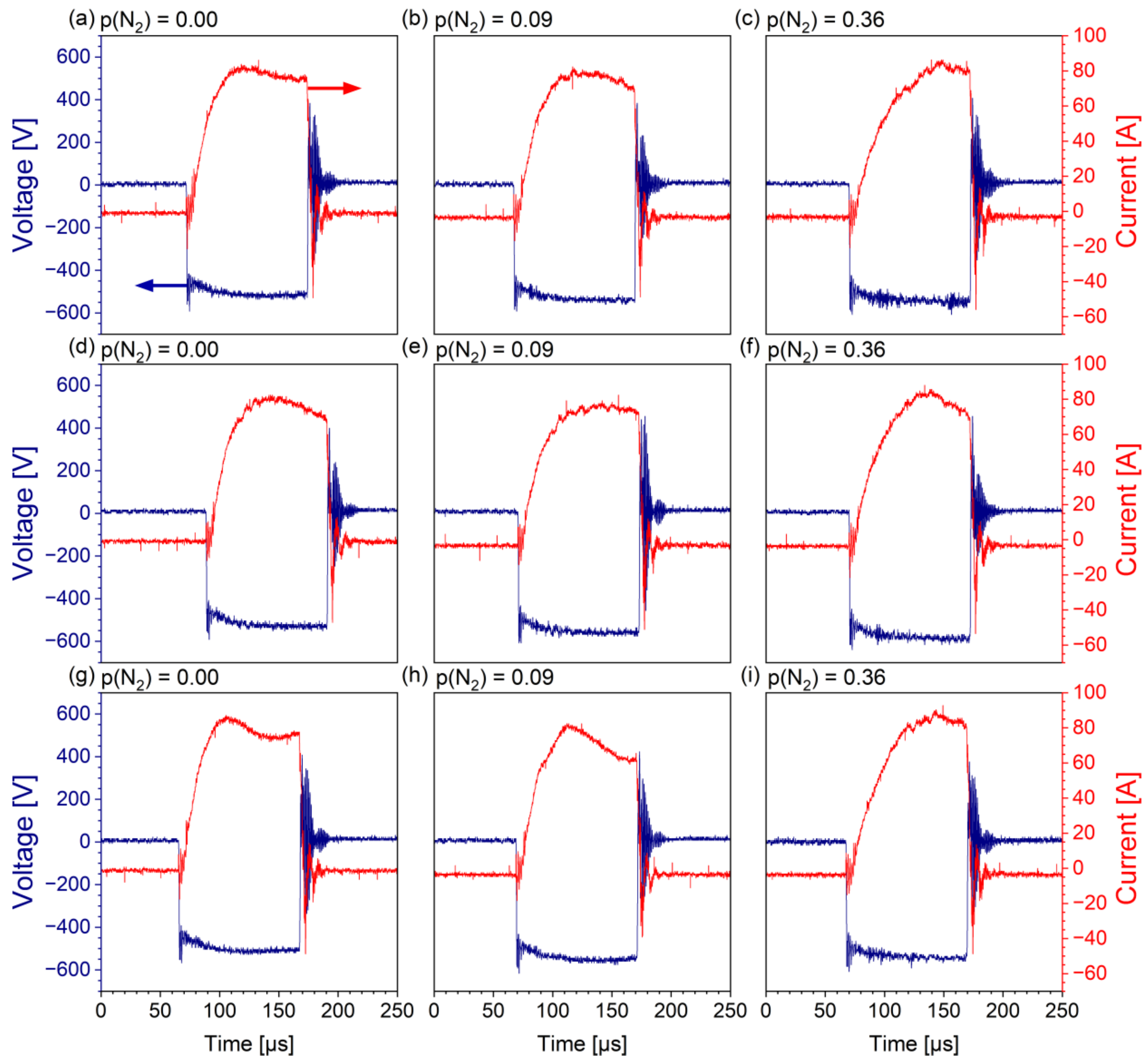

Figure 4-1: Current and voltage pulses of the HiPIMS discharge of: MoNbTaTiW (a) $p(N_2)$ = 0.00 Pa, (b) $p(N_2)$ = 0.09 Pa, (c) $p(N_2)$ = 0.36 Pa; CrMoNbTaW (d) $p(N_2)$ = 0.00 Pa, (e) $p(N_2)$ = 0.09 Pa, (f) $p(N_2)$ = 0.36 Pa and MoNbTaWZr (g) $p(N_2)$ = 0.00 Pa, (h) $p(N_2)$ = 0.09 Pa, (i) $p(N_2)$ = 0.36 Pa.

In Figure 4-2 the discharge voltage is shown. It was found that the discharge voltages of the films range between 520 – 680 V. The lowest discharge voltages were found for the MoNbTaTiW and MoNbTaWZr films and the highest for the MnMoNbTaW films. The ionization energy of the metals has a significant impact on the discharge current as it affects how quickly metal ions can be produced to transport the current. Since the average power was kept constant, the current and voltage of the HiPIMS discharge are directly related. This assertion remains valid exclusively if a substantial portion of the current is derived from metal ion recycling. Therefore, the ionization energy of the fifth alloying elements is a key to understanding the variations in current as only one element was altered across the several HEAs [60]. Similar ionization energies and discharge voltages are found for the elements Ti (6.83 eV), V (6.75 eV), Cr (6.77 eV)

Zr (6.63 eV), and Hf (6.83 eV) [61]. The same correlation can be found for the MnMoNbTaW films, which had the highest discharge voltage and the highest ionization energy for Mn (7.43 eV) [61]. In case of the MoNbTaTiW and MoNbTaVW films the discharge voltage increased with increasing $p(N_2)$. A similar behavior was already reported for depositing TiN using DCMS [62]. In contrary, no significant increase of the discharge voltage was found for MnMoNbTaW and HfMoNbTaW.

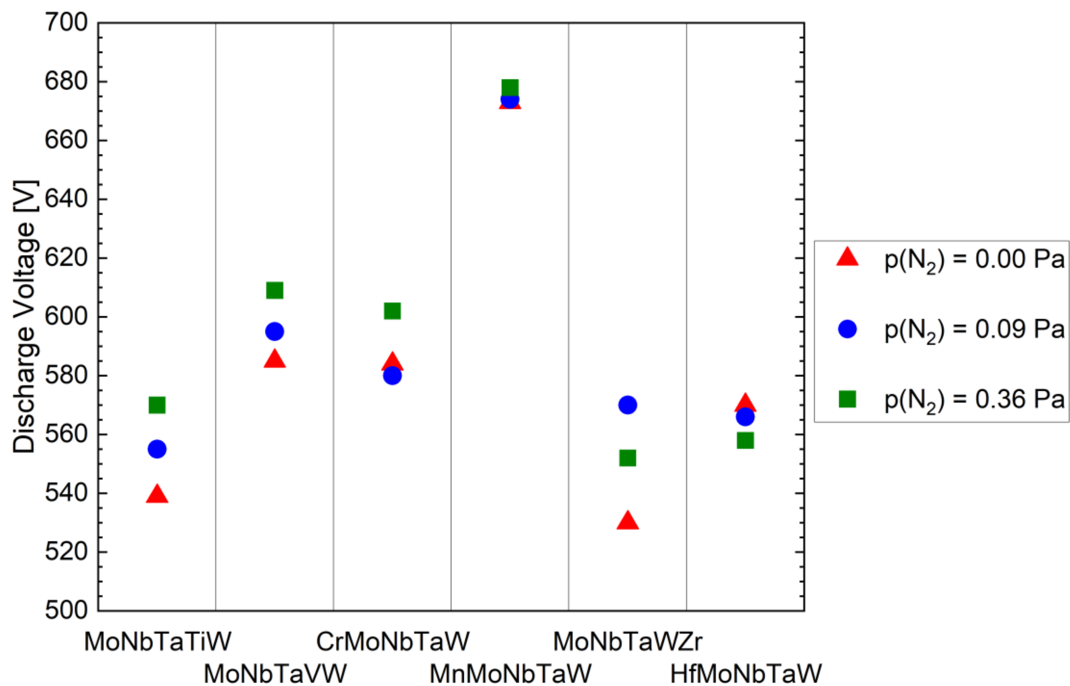

Figure 4-2: Discharge voltage of HEA films deposited with HiPIMS at different N_2 partial pressures after 30 min deposition time.

4.1.3. Film thickness and deposition rate

The film thickness and deposition rates are shown in Figure 4-3. Depending on the alloy and N_2 partial pressure, the film thicknesses range from 535 to 850 nm. Since the deposition time of 90 min was constant, the resulting deposition rate follows the same trend as the film thickness.

In general, all metal films ($p(N_2)$ = 0.00 Pa) are showing a lower deposition rate, compared to the films deposited in an N_2-containing atmosphere ($p(N_2)$ = 0.09 Pa or $p(N_2)$ = 0.36 Pa), with the exception of MoNbTaWZr and HfMoNbTaW deposited with higher N_2 partial pressures. The higher deposition rates for the nitrides can be explained by the additionally incorporated N-atoms into the lattice [18]. It is not fully understood, why MoNbTaWZr and HfMoNbTaW behave differently, but the lower deposition rate of the film deposited with the higher nitrogen pressure can be a sign for

target poisoning occurring at the higher nitrogen pressure. Additionally, Zr and Hf form exceptional stable nitrides [63], which may also influence the deposition rate. Another exception can be observed for the MnMoNbTaW nitrides, where the highest deposition rates were achieved.

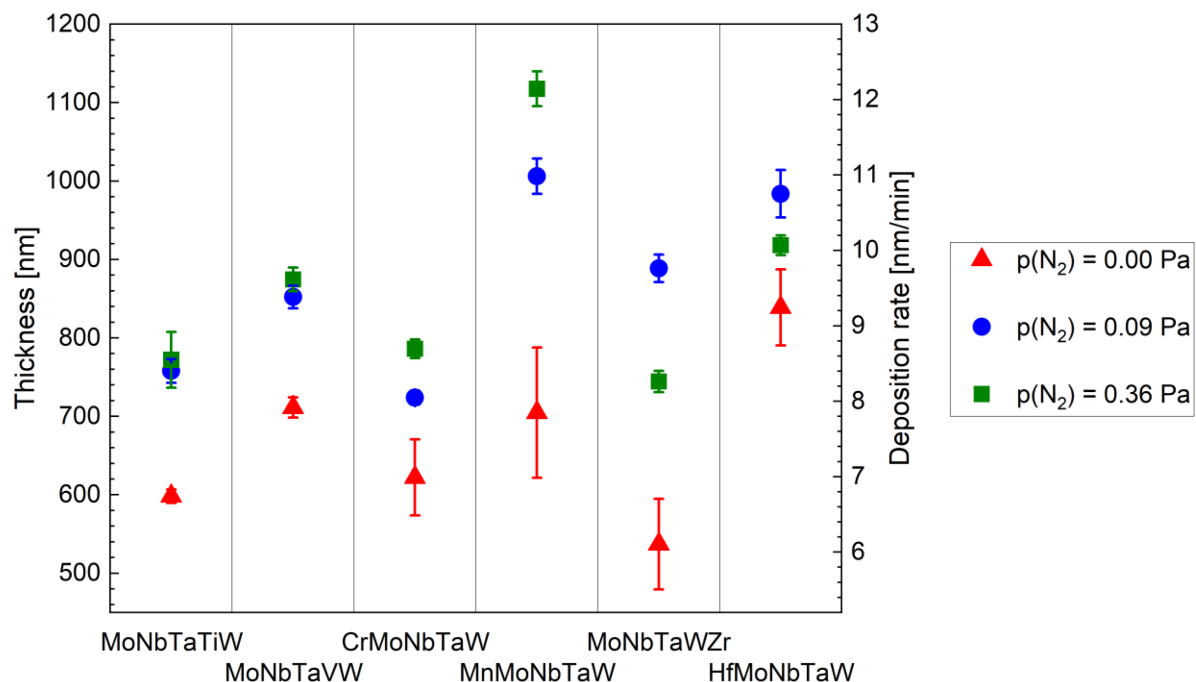

Figure 4-3: Film thickness and corresponding deposition rate of HEA films deposited with different N_2 partial pressures.

4.2. Film characterization

4.2.1. Chemical composition

The results derived by the EDX measurements are summarized in Table 2. In general, all metals can be divided into light (Ti, V, Cr, Mn), medium heavy (Zr, Mo, Nb) and heavy (Ta, W) metal elements, due to their atomic mass.

The concentration of the light metal elements in the alloys is always higher than the concentration of the medium heavy and heavy metal elements. This was also found by Xia et al. [39] when researching the angular-dependent deposition of MoNbTaVW HEA thin films. The authors have found an increased emission of lighter metal elements in the direction perpendicular to the target surface. Light metal elements are depleted at the target surface because they are scattered back by the heavy metal atoms after a single knock-on collision with the incoming ion. As a result, the lighter metal elements

are emitted from deeper regions within the target, leading to a more focused angular distribution [39].

For the films deposited with a low N_2 partial pressure ($p(N_2)$ = 0.09 Pa), the concentration of nitrogen varies between 22 at.% and 44 at.%. The nitrogen concentration of the films deposited with a high N_2 partial pressure ($p(N_2)$ = 0.36 Pa) indicates a nearly stoichiometric concentration of 50 at.% N_2. The only exception is MnMoNbTaW with 44 at.% and CrMoNbTaW with 45 at.% N_2. A possible explanation for the low nitrogen concentration in (MnMoNbTaW)N is the incorporation of nitrogen vacancies, as Mn prefers to form much more stable non-equimolar nitrides such as Mn_4N or Mn_3N_2 as a result of the reactive deposition process [64]. This can also be observed for Cr, which also forms Cr_2N in addition to CrN [65]. The small difference of the nitrogen concentration between both (MoNbTaTiW)N and (MoNbTaVW)N correlates with the similar deposition rates measured.

Table 2: Chemical composition of the as-deposited thin films.

MoNbTaTiW	**$p(N_2)$ = 0.00 Pa**	**$p(N_2)$=0.09 Pa**	**$p(N_2)$=0.36 Pa**
Element	[at.%]	[at.%]	[at.%]
N		42	49
Ti	27	17	13
Nb	21	12	10
Mo	21	12	10
Ta	16	11	9
W	16	7	9

MoNbTaVW	**$p(N_2)$ = 0.00 Pa**	**$p(N_2)$=0.09 Pa**	**$p(N_2)$=0.36 Pa**
Element	[at.%]	[at.%]	[at.%]
N		44	51
V	26	15	12
Nb	20	11	10
Mo	21	12	10
Ta	16	9	8
W	17	10	9

CrMoNbTaW	**$p(N_2)$ = 0.00 Pa**	**$p(N_2)$=0.09 Pa**	**$p(N_2)$=0.36 Pa**
Element	[at.%]	[at.%]	[at.%]
N		38	45
Cr	25	16	15
Nb	20	13	11
Mo	21	13	11
Ta	16	10	9
W	17	10	9

MnMoNbTaW	**$p(N_2)$ = 0.00 Pa**	**$p(N_2)$=0.09 Pa**	**$p(N_2)$=0.36 Pa**
Element	[at.%]	[at.%]	[at.%]
N		22	44
Mn	21	19	14
Nb	21	16	11
Mo	21	16	12
Ta	18	13	9
W	19	14	10

MoNbTaWZr	**$p(N_2)$ = 0.00 Pa**	**$p(N_2)$=0.09 Pa**	**$p(N_2)$=0.36 Pa**
Element	[at.%]	[at.%]	[at.%]
N		41	49
Zr	23	13	11
Nb	23	13	11
Mo	22	13	10
Ta	15	10	10
W	17	10	9

HfMoNbTaW	**$p(N_2)$ = 0.00 Pa**	**$p(N_2)$=0.09 Pa**	**$p(N_2)$=0.36 Pa**
Element	[at.%]	[at.%]	[at.%]
N		29	50
Nb	22	16	11
Mo	23	17	12
Hf	17	12	8
Ta	19	12	9
W	19	14	10

4.2.2. Microstructure

The microstructure of the films was obtained by XRD, the according diffractograms are shown in Figure 4-4. The theoretical peak positions, marked in Figure 4-4, were calculated assuming a Vegard's like behavior, with the help of the lattice parameters

$$a_{\mathrm{Vegard}} = \sum x_i a_i, \qquad (5.1)$$

where a_{Vegard} describes the calculated lattice constant and x_i the concentration of the element with lattice constant a_i [66]. The peak positions 2Θ were calculated according to

$$2\Theta = 2\sin^{-1}\left(\frac{\lambda_{Cu} * \sqrt{h^2 + k^2 + l^2}}{2a_{Vegard}}\right), \qquad (5.2)$$

where $\lambda_{Cu} = 1.5406$ Å describes the wavelength of Cu-K_α radiation and h, k and l the Miller indices of the diffracted plane [67]. The used lattice constants were reported by the International Centre for Diffraction Data (ICDD) for Ti [68], V [47], Cr [65], Mn [69], Zr [70], Nb [71], Mo [71], Hf [71], Ta [72] and W [73]. Since it is very difficult to distinguish between the different types of nitrides in the films, only MeN were used for the peak fitting. However, it should be noted that other nitrides, e.g., MeN_2 or Me_2N, are also possible and must be considered for further research. Just like the metals, the lattice constants of nitrides were reported by the ICDD for TiN [74], VN [75], CrN [76], MnN [77], ZrN [78], NbN [79], MoN [80], HfN [81], TaN [82] and WN [83].

The metallic films exhibit a bcc microstructure characterized by a favored orientation along the (110) plane.It was found, that the metal MoNbTaWZr film has an amorphous structure (Figure 4-4 (e)). Most of the HEA nitride films are characterized by a fcc NaCl structure. In case of the films deposited with a lower nitrogen partial pressure, mostly a dominant (111) peak and a less intense (200) peak was found. Only the (MnMoNbTaW)N and (HfMoNbTaW)N film show an amorphous structure. The microstructure of (MnMoNbTaW)N (Figure 4-4 (d)) is completely amorphous and in case of (HfMoNbTaW)N (Figure 4-4 (f)) partly amorphous. This, however, can be explained with the low nitrogen content within the film, see Table 2. An amorphous structure of HEN films with lower nitrogen contents was also found by Xia et al. [46] for (MoNbTaVW)N films. The films deposited with a higher nitrogen partial pressure also have a fcc structure but mainly the (111) peak can be seen in the X-ray diffractograms (Figure 4-4). In contrast to the fcc peaks of the films deposited with a lower nitrogen

partial pressure, the peak position of the films deposited deviates less from the calculated position gained by Vegard's-like behavior. This can be explained with the lower nitrogen content found in the films deposited with a lower nitrogen partial pressure and therefore suggests nitrogen vacancies in the lattice structure.

Figure 4-5 summarizes the dependency of the nitrogen-concentration of the films and the corresponding microstructure. It is worth noting that the colored areas were estimated, and the influence of the deposition parameters must be considered. Additionally, it was found that the MoNbTaWZr film has an amorphous structure in the metallic state.

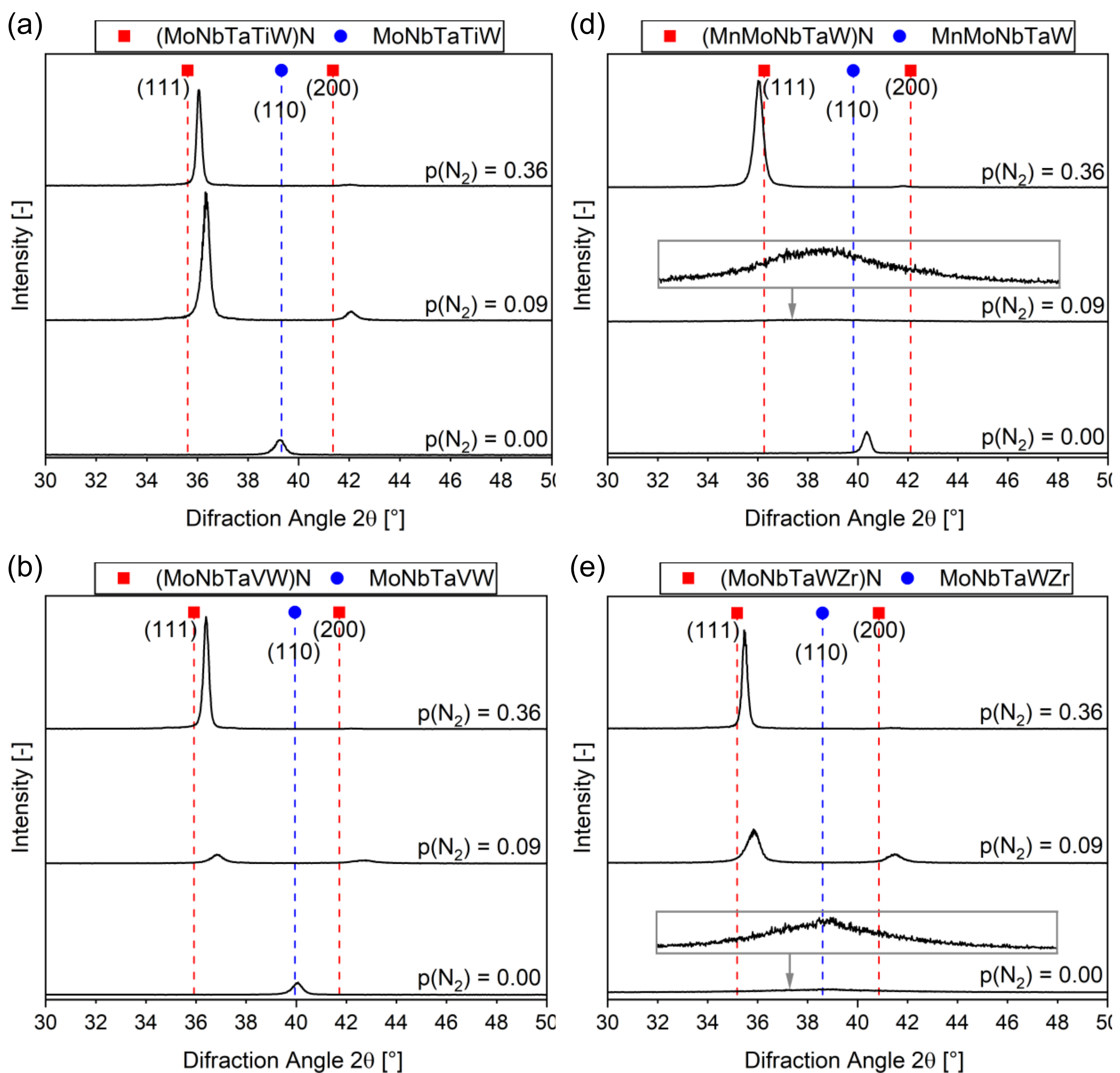

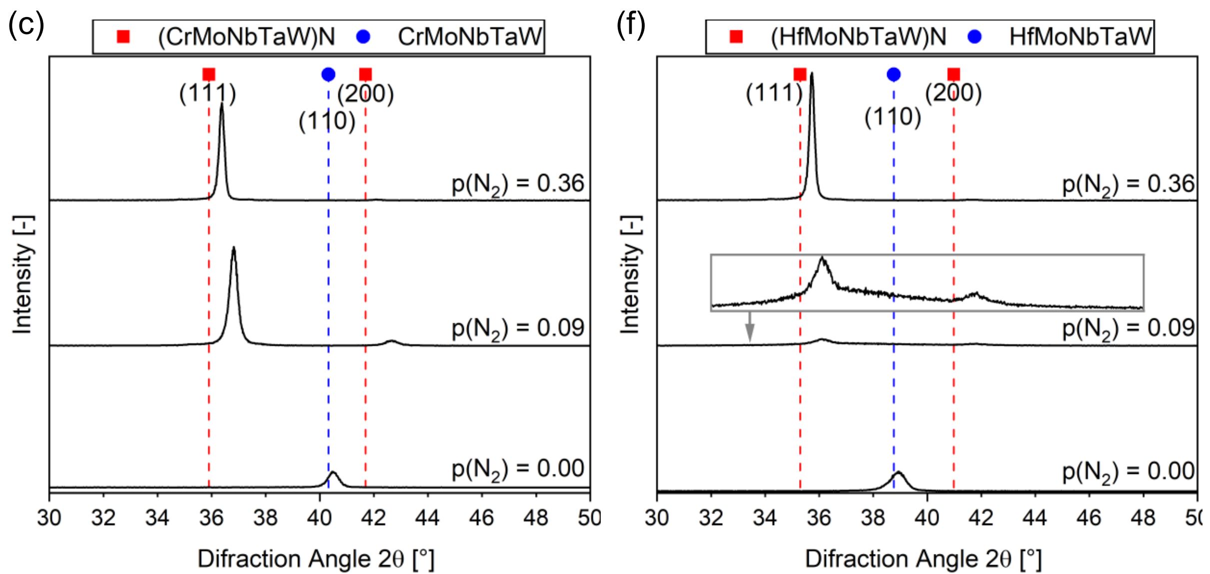

Figure 4-4: X-ray diffractograms of the as-deposited films for (a) MoNbTaTiW, (b) MoNbTaVW, (c) CrMoNbTaW, (d) MnMoNbTaW, (e) MoNbTaWZr, (f) HfMoNbTaW deposited with different nitrogen partial pressures. Additionally, in (d), (e) and (f) enlarged inserts can be found.

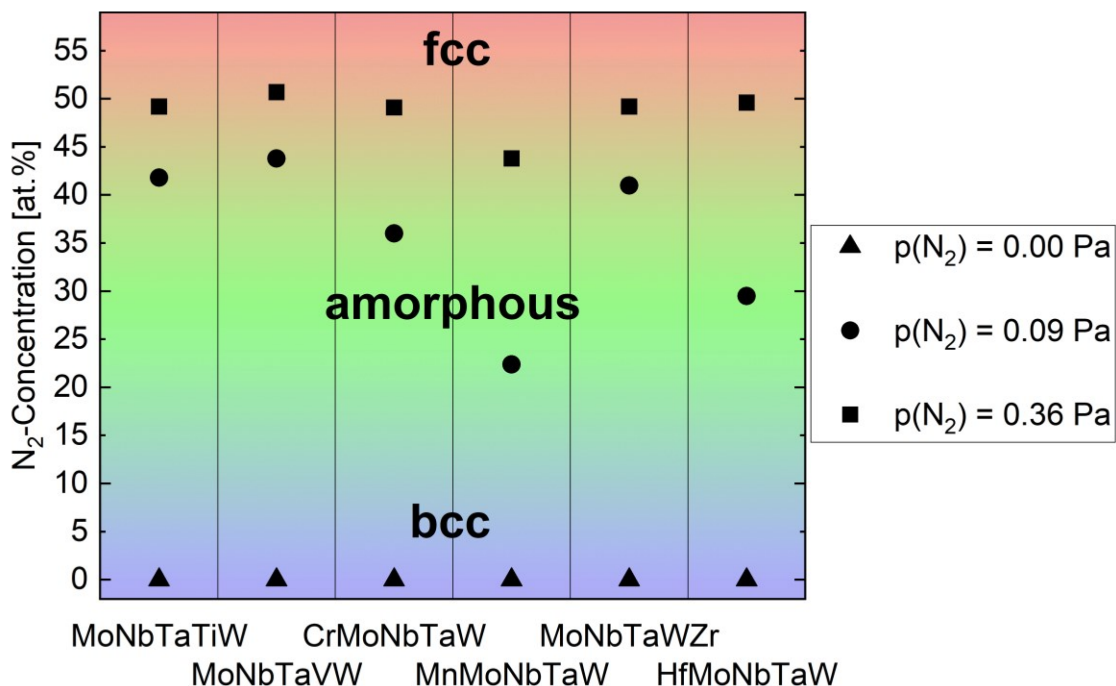

Figure 4-5: Comparison of N_2-concentration and resulting microstructure. The metal MoNbTaWZr film shows an amorphous structure, since Zr suppresses the formation of a bcc microstructure.

In addition to the XRD investigations, two (MoNbTaTiW)N samples, deposited on TEM-grids, were analyzed by TEM. In Figure 4-6 (a) and (c), bright field (BF) images of (MoNbTaTiW)N are shown. Both films show a dense, nanocrystalline microstructure.

The SAED images in Figure 4-6 (b) and (d) reveal a fcc microstructure for both films, which is consistent with the results of the XRD measurements. A comparison of the

lattice parameters obtained by SAED and XRD is shown in Table 3. It was found that, the difference in the calculated results is marginal.

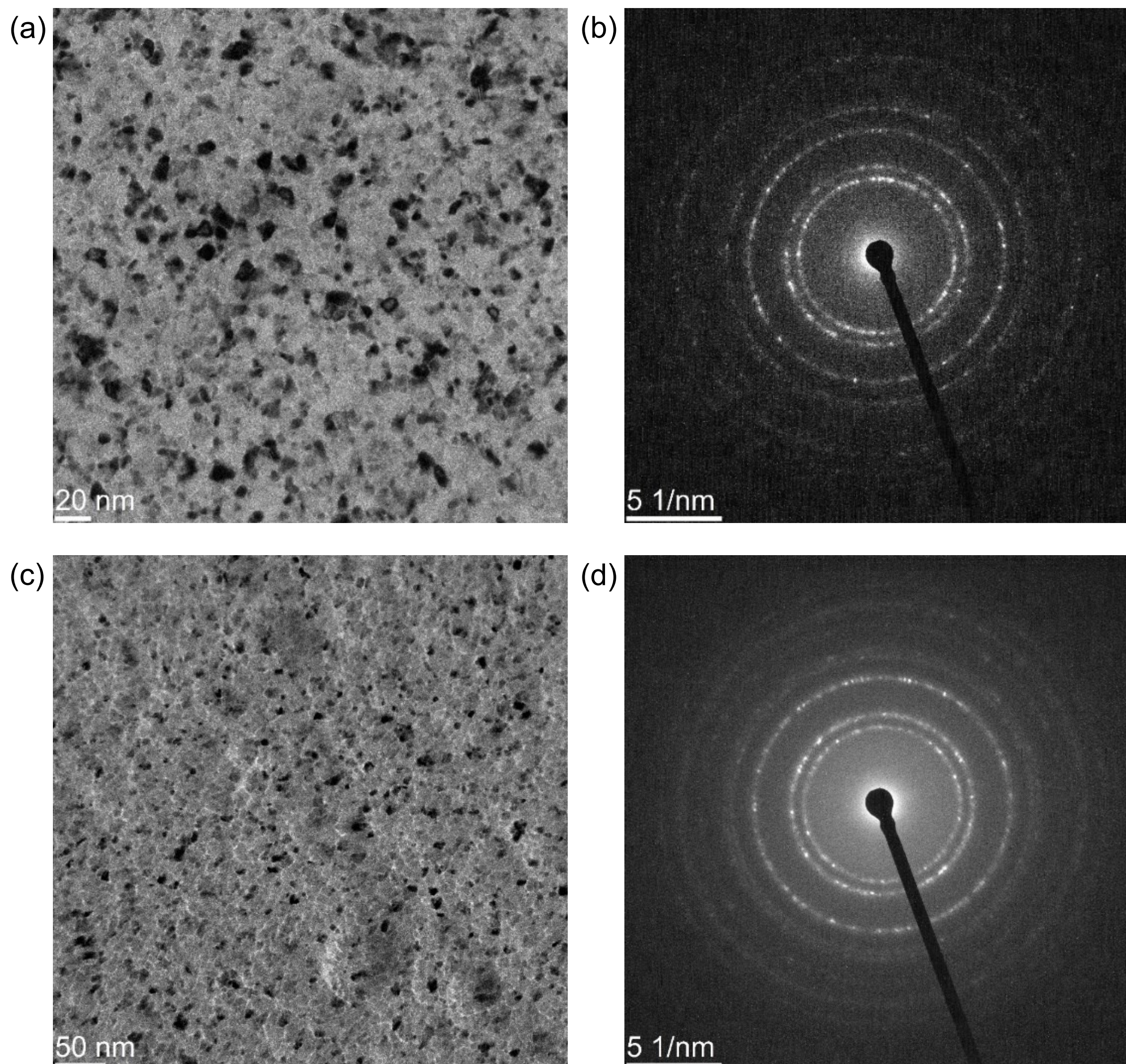

Figure 4-6: TEM BF surface images of as-deposited (MoNbTaTiW)N films deposited with a N_2 partial pressure of (a) 0.09 Pa and (c) 0.36 Pa. The corresponding SAED pattern are shown in (b) and (d).

Table 3: Comparison of the lattice parameters obtained by XRD and SAED analysis for (MoNbTaTiW)N.

MoNbTaTiW	a_{SAED} **[Å]**	a_{XRD} **[Å]**
p(N_2) = 0.09 Pa	4.265	4.281
p(N_2) = 0.36 Pa	4.245	4.311

4.2.3. Electrical properties

The results obtained by the electrical resistivity measurements are shown in Figure 4-7. The resistivity of the metal films is the smallest and increases with the nitrogen content, as the ratio of the ceramic MeN bonds increases. This is expected, as

ceramics tend to have lower electric conductivity compared to metals [84]. It was found that the resistivity of the metal films ranges between 70 µΩcm for the CrMoNbTaW film and 175 µΩcm for the MoNbTaWZr film. An explanation for the higher resistivity of the MoNbTaWZr metal film might be its amorphous microstructure. According to Matthiessen's rule, the resistivity of amorphous films is higher because of the stronger scattering of the electrons at defects [85]. In comparison, the resistivity of the films deposited at a low nitrogen pressure increases by a factor of 4 to values ranging from 235 µΩcm for the (MnMoNbTaW)N film to 634 µΩcm for the (MoNbTaWZr)N film. Although the low nitrogen containing (MnMoNbTaW)N films shows an amorphous structure, the measured resistivity was the lowest compared to the other films deposited with the low nitrogen partial pressure. This can be explained with the low nitrogen content of 22 at.% in the film (Table 2). The electrical resistivity additionally doubles for the films deposited at the high nitrogen content. However, the (MoNbTaWZr)N and (HfMoNbTaW)N films with high nitrogen content showed extremely high resistivity values of 2564 µΩcm and 2132 µΩcm, respectively. It is currently not fully understood why these high values were measured but they may indicate underdense films.

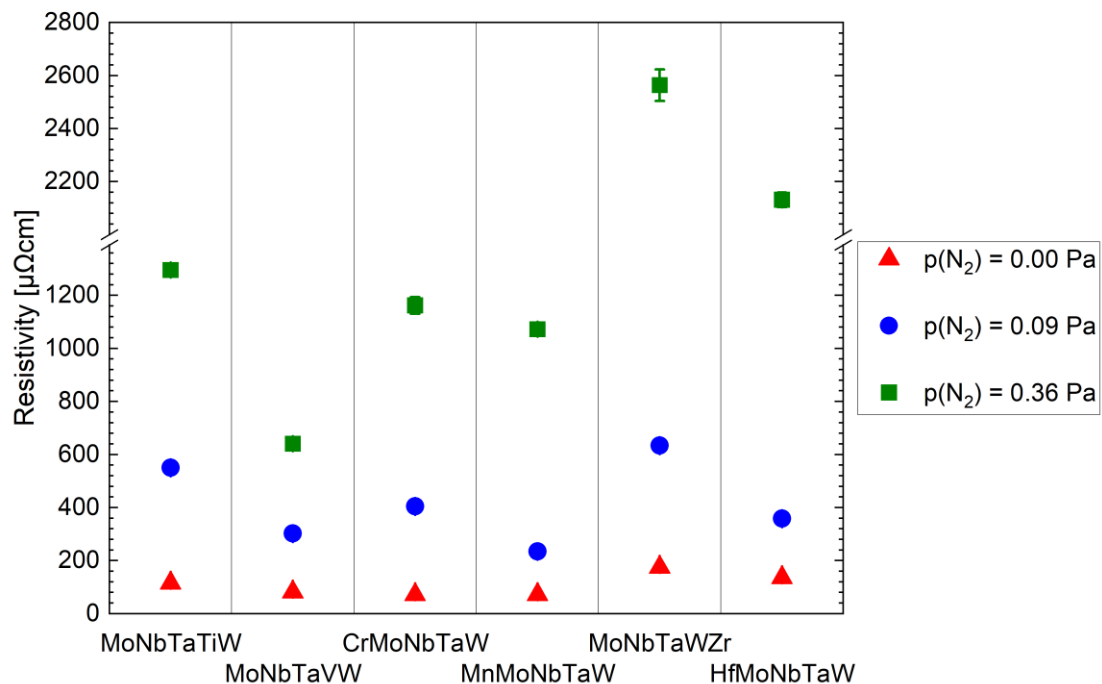

Figure 4-7: The electrical resistivity of the as-deposited HEA and HEN films.

4.2.4. Residual stress

In Figure 4-8 the results of the residual stress measurements conducted by using the wafer curvature method are shown. All films have tensile stresses, which vary from 73 MPa to 1376 MPa. These stresses were possibly caused by growth stresses, e.g. stemming from ion bombardment during film deposition, and thermal stresses. A trend in the residual stress was observed for the HENs containing Ti, V, Cr, and Mn deposited at the low nitrogen partial pressure, which could be explained by the decreasing atomic radii of the fifth element. The metal films generally displayed the highest tensile stresses, followed by films deposited at $p(N_2)$ = 0.09 Pa and the lowest for those deposited at $p(N_2)$ = 0.36 Pa. A possible explanation for the decrease of residual stresses with increasing nitrogen-content could be the incorporation of nitrogen interstitials, which cause compressive residual stresses that superimpose with tensile residual stresses [86]. In general nitride films tend to have compressive residual stresses [87]. Since no bias voltage was applied during deposition, the occuring tensile residual stresses can be explained. However, there were some exceptions to this trend. For example, the (MoNbTaWZr)N film deposited at $p(N_2)$ = 0.09 Pa had the lowest residual stress compared to other Zr-containing films, while the HfMoNbTaW metal film had the lowest residual stress of all as-deposited metal films.

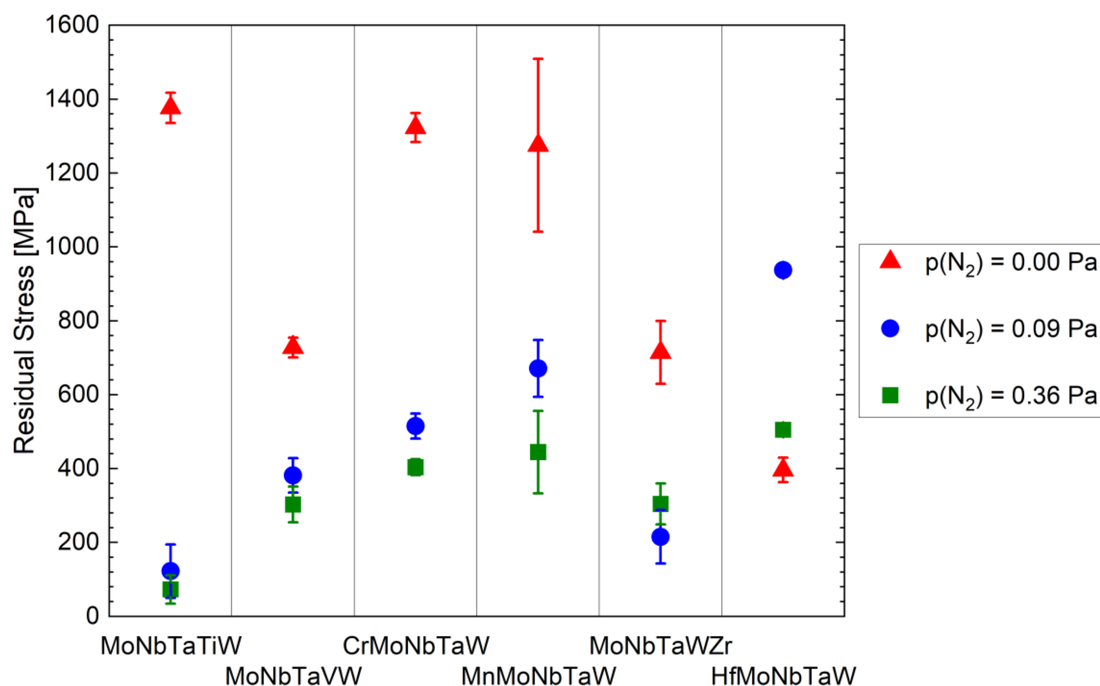

Figure 4-8: Residual stress of the as-deposited HEA and HEN films.

4.3. Thermal stability

4.3.1. Chemical composition

The chemical composition of the (CrMoNbTaW)N films after annealing was measured using EDX. This was done to determine if the chemical composition changes during annealing in vacuum. The results of these measurements can be seen in Table 4. Despite minor deviations, caused by the measurement method and the deposition process, the overall composition of the films remained constant after annealing, indicating that these HEA nitride films are chemically stable up to a temperature of 900 °C. MoNbTaTiW, MoNbTaVW, and CrMoNbTaW HEA films have already been reported by Gruber et al. [88] to be chemically stable up to 1000 °C, which corresponds to the results summarized in Table 4.

Table 4: Chemical composition of (CrMoNbTaW)N films after annealing.

	(CrMoNbTaW)N, $p(N_2)$=0.09 Pa				(CrMoNbTaW)N, $p(N_2)$=0.36 Pa			
Element	25 °C [at.%]	500 °C [at.%]	700 °C [at.%]	900 °C [at.%]	25 °C [at.%]	500 °C [at.%]	700 °C [at.%]	900 °C [at.%]
N	38	38	39	39	45	46	45	44
Cr	16	16	15	15	15	14	14	14
Nb	13	13	13	12	11	11	11	11
Mo	13	13	13	13	11	11	11	11
Ta	10	10	10	10	9	8	9	9
W	10	10	11	11	9	9	9	10

4.3.2. Microstructure

The X-ray diffractograms of the CrMoNbTaW based films after annealing at 500 °C, 700 °C and 900 °C are shown in Figure 4-9. These diffractograms are representative for the results obtained for the other alloys, which can be found in the appendix. The exceptions are described in the second part of this chapter. Generally, the microstructure of the films does not seem to be significantly affected by the annealing treatment. However, a noticeable trend, that can be observed in all the XRD-patterns, is a gradual peak shift towards higher diffraction angles. The peak shifts away from the projected peak position as temperature rises, contrary to what is anticipated. This may be explained by the fact that the peak location was calculated according to Vegard's-like behavior, and particularly in the case of films deposited at low nitrogen partial pressure, the equilibrium lattice constant already resides elsewhere since this lattice is smaller and contains vacancies. This shift is believed to indicate a stress relief in the

films, which may be caused by the relaxation of internal stresses and the elimination of defects during the annealing, resulting in a smaller volume of the lattice.

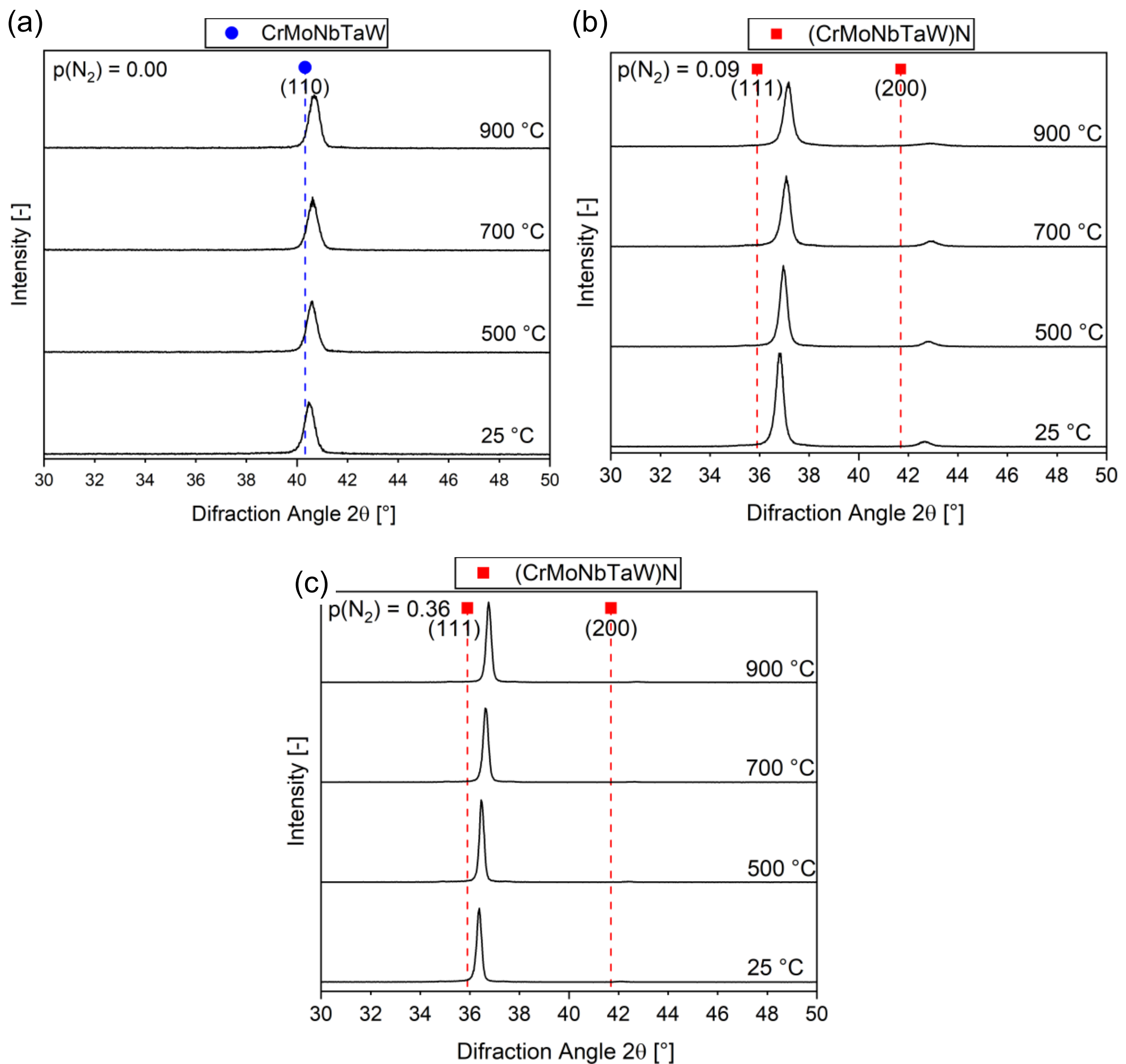

Figure 4-9: X-ray diffractograms of CrMoNbTaW in the as-deposited state (25 °C) and after annealing at 500 °C, 700 °C and 900 °C for (a) p(N_2) = 0.00 Pa, (b) p(N_2) = 0.09 Pa and (c) p(N_2) = 0.36 Pa.

The (MnMoNbTaW)N film deposited with a p(N_2) = 0.09 Pa (Figure 4-10 (a)) and the metal MoNbTaWZr film (Figure 4-10 (c)) was initially found to have an amorphous microstructure. However, upon annealing at a temperature of 900 °C in case of (MnMoNbTaW)N the film crystallizes and forms a fcc structure. In contrary, the metal MoNbTaWZr film starts to crystallize in a bcc crystal structure starting at 500 °C, when a small peak can be observed. The (HfMoNbTaW)N deposited at p(N_2) = 0.09 Pa was found to be partly amorphous at 25 °C. However, it was found that no significant crystallization of the film occurred (Figure 4-11 (b)). When annealing the high nitrogen containing (MoNbTaWZr)N film at 900 °C a peak separation of the (111) peak

appeared. This may indicate the formation of a second phase or might be related to an inhomogeneous stress distribution, which was already reported by Gruber et al. [88] when investigating the thermal stability of MoNbTaTiW, MoNbTaTiW and CrMoNbTaW thin films. Another possibility might be the formation of an oxide, due to an insufficient vacuum during annealing. Thus, additional research is needed to fully understand this behavior.

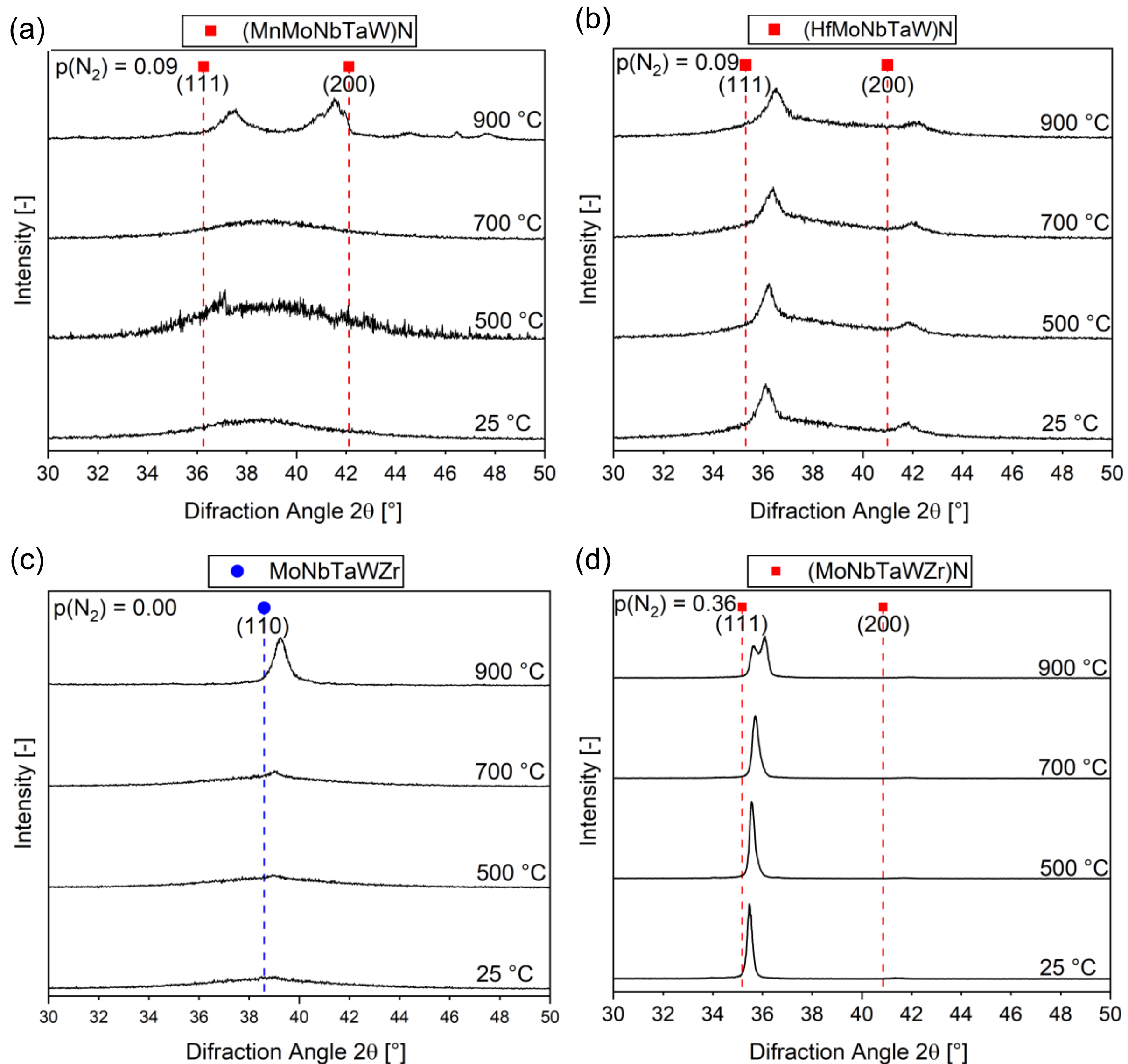

Figure 4-10: X-ray diffractograms of HEA and HEN films in the as-deposited state (25 °C) and after annealing at 500 °C, 700 °C and 900 °C of (MnMoNbTaW)N deposited at $p(N_2)$ = 0.09 Pa, (b) (HfMoNbTaW)N deposited at $p(N_2)$ = 0.09 Pa, (c) MoNbTaWZr deposited at $p(N_2)$ = 0.00 Pa and (d) (MoNbTaWZr)N deposited at $p(N_2)$ = 0.36 Pa.

4.3.1. Surface morphology

In Figure 4-11, the surface images of (CrMoNbTaW)N after annealing at different temperatures are shown. These images were obtained using CLSM. It was found that the nitride films experienced cracking during the annealing. The number of cracks increases with increasing annealing temperature. In addition, for some films deposited at higher nitrogen partial pressures local delaminations were observed (as seen in Figure 4-11 (b)). The formation of cracks is attributed to the presence of tensile residual stresses (see section 4.2.4), while delaminations are believed to arise from the contraction of the entire sample during the cooling process. Consequently, the cracks undergo closure, and in some instances, exhibit an enhanced closure beyond their initial state. The metal films did not crack during annealing. However, complete delamination was observed for the metal MoNbTaTiW and HfMoNbTaW films when annealed at 900 °C, as well as for the metal MnMoNbTaW film when annealed at 500 °C.

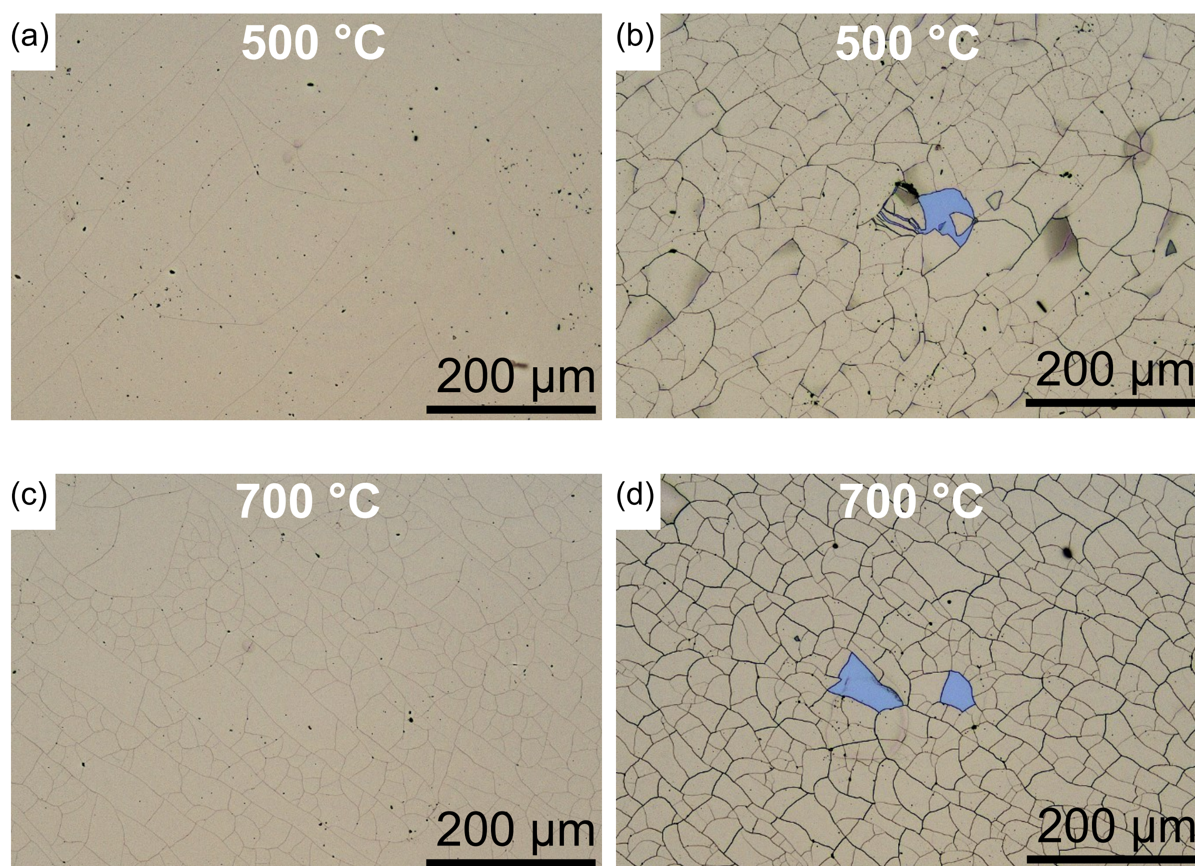

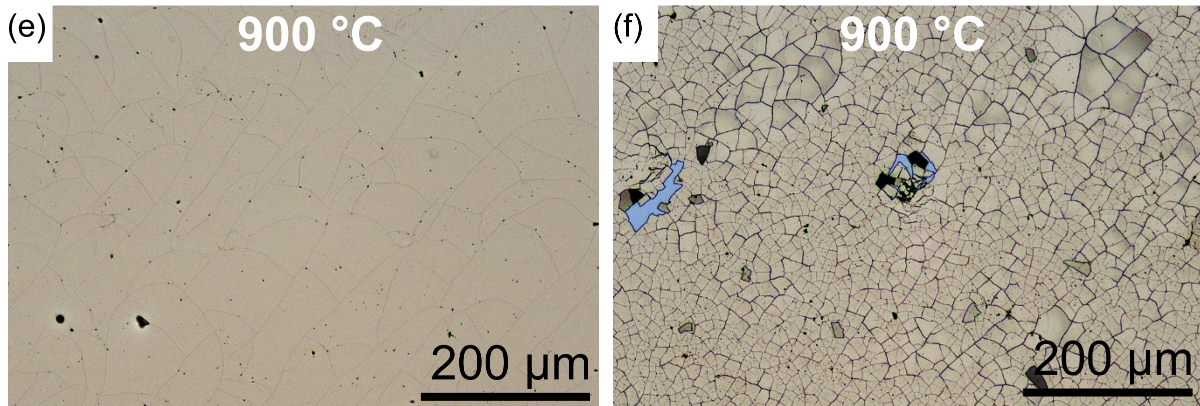

Figure 4-11: CLSM surface images after annealing of (CrMoNbTaW)N deposited at $p(N_2)$ = 0.09 Pa (a), (c), (e) and $p(N_2)$ = 0.36 Pa (b), (d), (f).

4.3.1. Electrical properties

The electrical resistivity after annealing is shown in Figure 4-12. In some cases, the resistivity was too high due to crack formation or delamination during annealing. While the resistivity of the metal films remained widely unchanged after annealing, the resistivity of the nitride films significantly increased with annealing temperature. This increase can be attributed to the formation of cracks, as shown in Figure 4-11, which disrupt the smooth flow of electrons and increases the resistivity of the films. The current can only flow through the areas where the cracks are in contact, resulting in a reduction of the effective cross section area available for current conduction. It can be observed that the increase in electrical resistivity of the films deposited at higher nitrogen partial pressures is more pronounced compared to the films deposited at lower partial pressures nitrogen. This behavior can be explained with the higher crack density of the films deposited at higher partial pressure nitrogen (Figure 4-11 (a)) compared to the films deposited at lower nitrogen partial pressures (Figure 4-11 (b)) When annealing the metal MoNbTaWZr film (Figure 4-12 (e)) and the low nitrogen containing (MnMoNbTaW)N film (Figure 4-12 (d)) at 900 °C, a significant decrease in resistivity was observed. This can be explained with the transformation from amorphous to a crystalline bcc phase as observed by XRD shown in Figure 4-10 (c) for the MoNbTaWZr film and in Figure 4-10 (a) for the low nitrogen containing (MnMoNbTaW)N film.

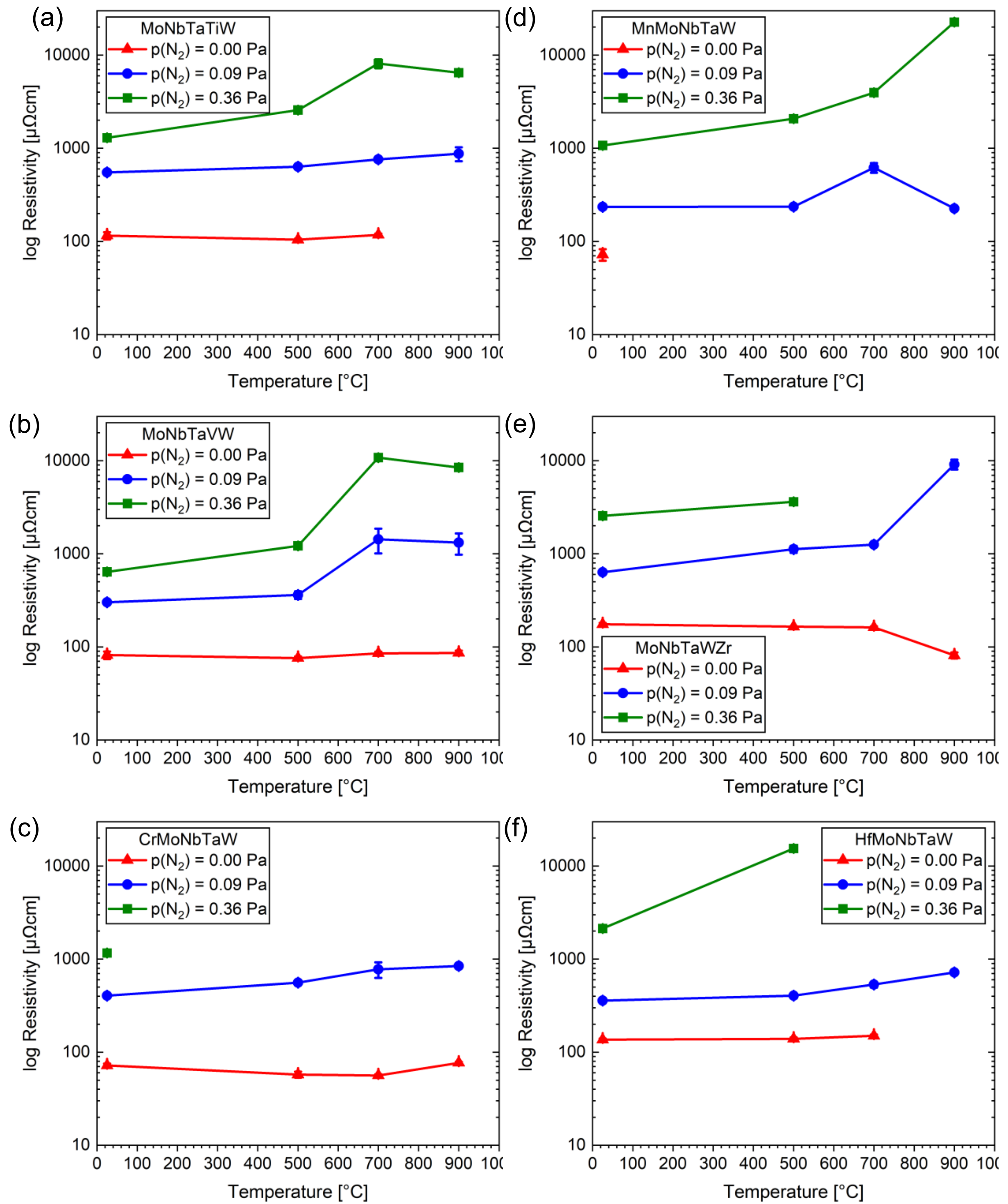

Figure 4-12: Resistivity after annealing of (a) MoNbTaTiW, (b) MoNbTaVW, (c) CrMoNbTaW, (d) MnMoNbTaW, (e) MoNbTaWZr and (f) HfMoNbTaW films.

4.3.2. Residual stress

In Figure 4-13 the residual stress of the metal films after annealing is shown. Since all the nitride films cracked during annealing, they are not presented in this section. Cracking leads to a stress relief in the films and therefore the results of those measurements are not representative of the residual stresses within the nitride films.

In case of MoNbTaTiW a significant increase of the residual stress was noticed after annealing to 500 °C. Annealing to higher temperatures resulted in a nearly linear decrease to the value measured for the as-deposited film. A similar but less pronounced trend was noticed for the HfMoNbTaW film but due to delamination a measurement after annealing at 900 °C was not possible. A slight decrease of the residual stress was observed for the MoNbTaVW film. The residual stress of the CrMoNbTaW film increased with increasing annealing temperatures. In case of the MoNbTaWZr the stress firstly peaked at 500 °C, dropped at 700 °C and peaked again at 900 °C.

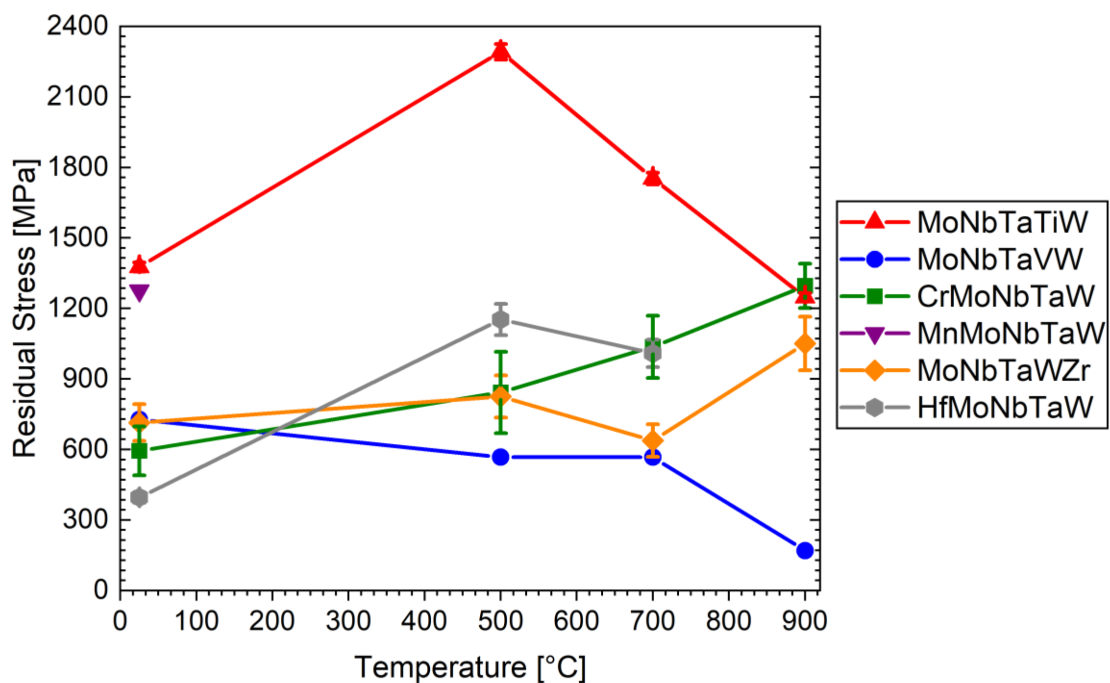

Figure 4-13: Residual stress after annealing.

4.3.3. In-situ Stress Measurements

To better understand the stress relaxation mechanisms, in-situ stress measurements using the wafer curvature method were done. The results will be discussed on the basis of the CrMoNbTaW and (CrMoNbTaW)N films, since they are representative for the results of the other films. The results obtained for the other films can be found in the appendix of this thesis.

Figure 4-14 illustrates the evolution of the residual stress in the CrMoNbTaW metal film. The measurement starts with an initial stress of around 1070 MPa and quickly decreases. At around 100°C, a small hump appears, indicating the end of the thermo-elastic region. The stress further changes into the compressive region until reaching 650 °C. At around 650°C a plateau is noticeable, which is followed by a stress decrease until the maximum temperature of 810 °C is reached. This decrease can be explained by non-elastic deformation, including annihilation of defects, gliding of dislocations, and relaxation of grain boundaries [56]. During cooling, the stress increases until approximately 780 °C and decreases until 630 °C. It is expected that thermal tensile stresses would build. However, the temperature is so high that stress relaxation is possible due to e.g., dislocation movement. Therefore, the system wants to be in a stress-free state as much as possible. Above about 650°C, thermal activation is no longer sufficient and thermal tensile stresses build up. After the stress decrease the stresses increase again according to a thermo-elastic behavior. The cycle ends at a similar stress value as it has started. The second thermo-cycle begins again with a thermo-elastic behavior, which lasts up to 650 °C. Although the stresses in the beginning of the second cycle are similar to the stresses at the beginning of the first cycle, the lowest compressive stresses, reached within the second cycle. are lower compared to the compressive stresses reached during the first one. When the temperature is further increased the stresses are decreasing again, indicating that stress relaxation processes were not completed after the first cycle. The reason for this inhibited stress relaxation behavior could be the sluggish diffusion effect of HEAs [32]. The cooling part of this cycle is quite similar to the one of the first cycle, but the tensile stresses in the end of this cycle were higher compared to the tensile stresses of the as-deposited films, which may be explained by a volume reduction during annealing.

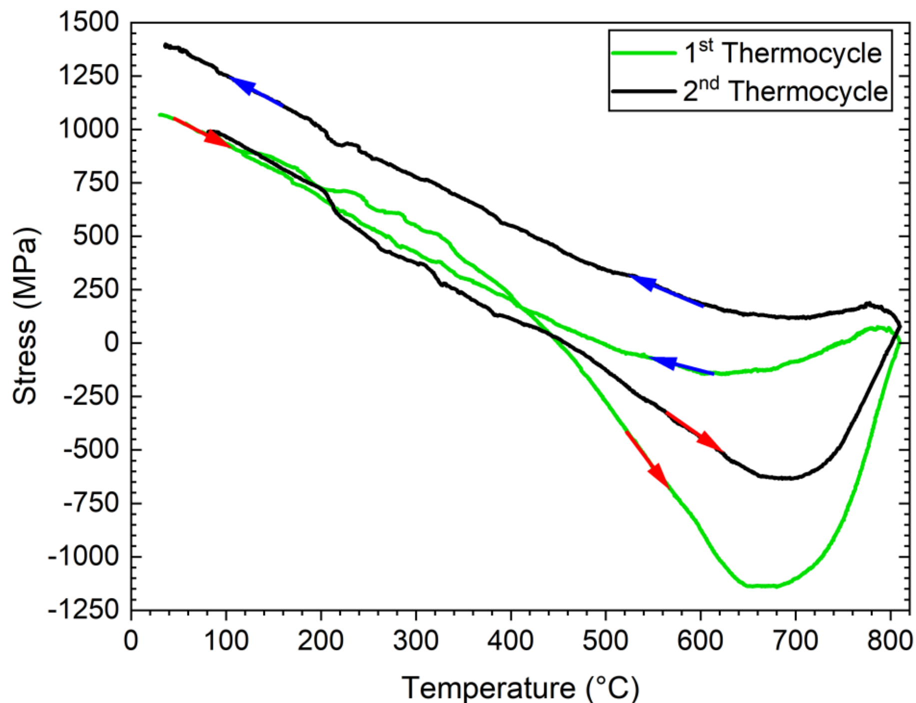

Figure 4-14: Stress-temperature curve of the metal CrMoNbTaW film.

The stress measurement of the (CrMoNbTaW)N film deposited with a nitrogen partial pressure of 0.09 Pa is shown in Figure 4-15. The stress quickly drops in the beginning of the thermocycle until approximately 150 °C, indicating the end of the thermo-elastic behavior. Even though no heating was involved during the deposition of the films, the temperature of the substrate increased during the deposition due to plasma heating. In case of the discussed (CrMoNbTaW)N the temperature reached about 120°C, which was measured with a thermocouple attached to the substrate holder. Once this point is reached, the stress continues to decrease until the temperature reaches 150°C. From 150 °C to 650 °C, the tensile stress level increases until it reaches a local maximum of 1175 MPa. This stress increase is most probably caused by defect annihilation, such as the combination of nitrogen interstitials into nitrogen vacancies, resulting in volume shrinkage. After reaching the local maximum, the stress decreases linearly until 810 °C with a similar slope as in the beginning of the measurement, indicating a thermo-elastic behavior. During cooling the stresses increase linearly, indicating a thermo-elastic behavior. Unfortunately, at 200 °C the measurement was terminated due to the high residual stresses.

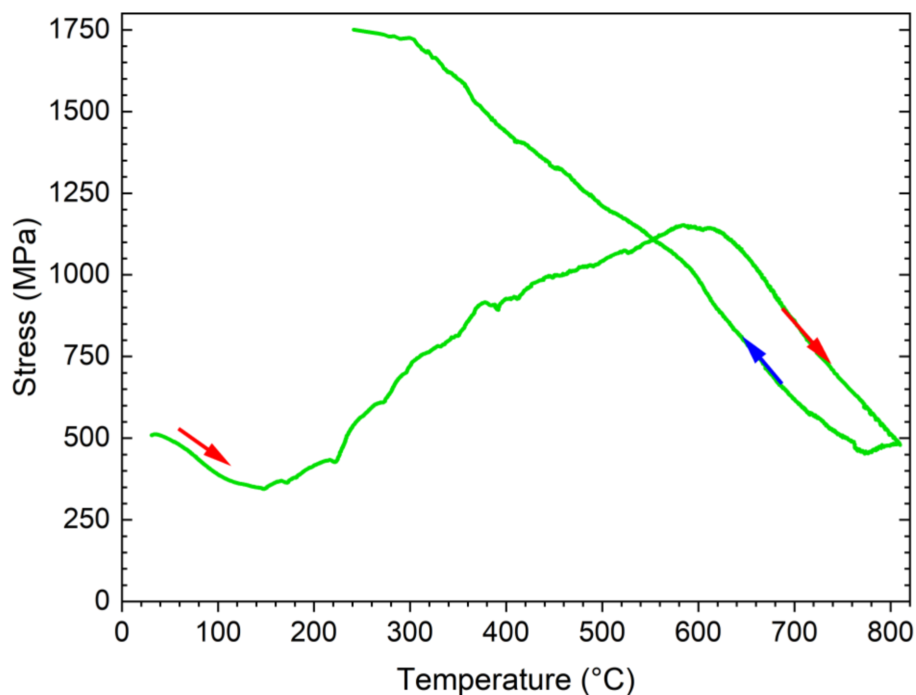

Figure 4-15: Stress-temperature curve of the (CrMoNbTaW)N film deposited at $p(N_2)$ = 0.09 Pa.

Figure 4-16 shows the stress evaluation of the (CrMoNbTaW)N film deposited with a nitrogen pressure of 0.36 Pa during annealing. The stress decreases linearly up to 150 °C according to the thermo-elastic behavior. After this decrease, the stress increases until reaching a stress maximum at 500 °C. Similar to the films deposited at a lower nitrogen partial pressure, a volume shrinkage of the film and annihilation of defects occurs. After further annealing, the stress decreases significantly, which is thought to be due to cracking. When the maximum temperature is reached, the cooling process proceeds linearly to room temperature. It was found that the cooling cycle slope had changed in comparison to the slope observed at the start of the annealing, thus providing evidence to support the notion of a cracked film. During the second thermal cycle, there were no significant alterations as the stress gradually decreased to 0 MPa and then increased to 260 MPa when cooled to room temperature in a linear manner due to cracking.

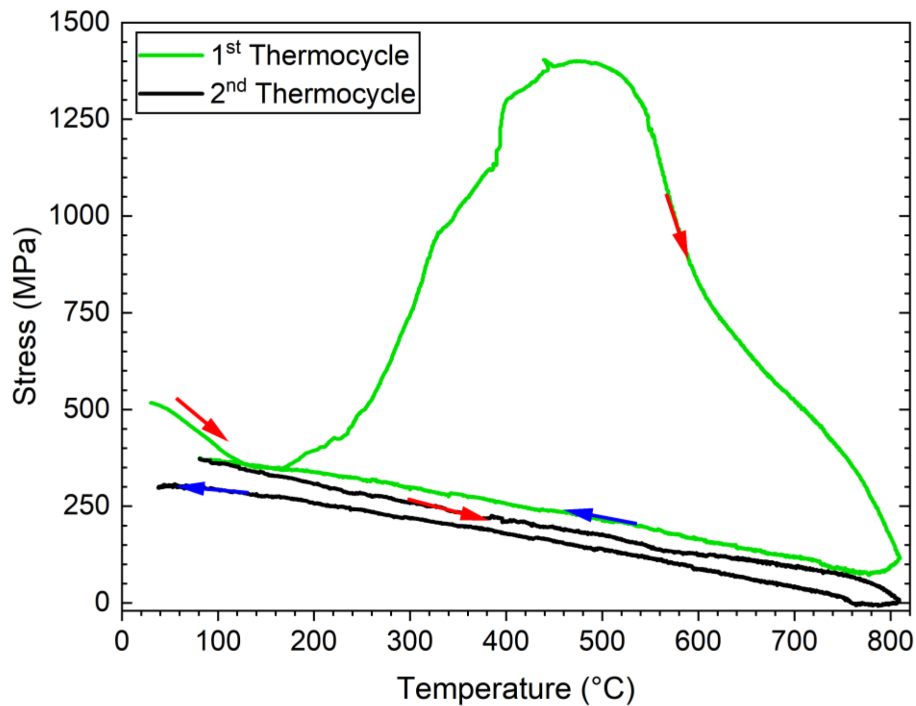

Figure 4-16: Stress-temperature curve of the (CrMoNbTaW)N film deposited at $p(N_2)$ = 0.36 Pa.

As a conclusion, it was found that even at very low temperatures, all HENs exhibit some degree of recovery, which is surprising considering that these alloys consist of refractory metals and recovery processes typically require much higher temperatures. Thus, it is believed that mainly the thermal movement of nitrogen and vacancies during annealing is the driving force of recovery, leading to a volume contraction in the film, resulting in tensile stresses in the films. When comparing the film with low nitrogen content to the one with higher nitrogen content, this effect is even more noticeable due a higher amount of nitrogen.

5. Conclusions

This thesis primarily focuses on a comparative investigation of thin films based on MoNbTaW high entropy alloy (HEA) and (MoNbTaW)N high entropy metal nitrides (HEN) deposited using HiPIMS at varying nitrogen pressures. The study revealed a gradual transition in microstructure from a bcc (body centered cubic) to fcc (face centered cubic) lattice with the incorporation of nitrogen. Moreover, the incorporation of insufficient nitrogen resulted in an amorphous microstructure.

Regarding the thermal stability of the films, all samples demonstrated chemical stability up to 900°C. However, the HEN films exhibited cracking during annealing due to high residual stresses, while the metal films experienced delamination in a few instances, but cracking was not observed in them.

Based on the findings from this study, the nitride films exhibit promising potential as hard coatings due to their remarkable thermal stability. Further investigations are warranted to evaluate their suitability as diffusion barriers in high-power electronic applications.

6. References

[1] M.C. Gao, J.-W. Yeh, P.K. Liaw, Y. Zhang, High-Entropy Alloys, Springer International Publishing, Cham, 2016. https://doi.org/10.1007/978-3-319-27013-5.

[2] B. Cantor, I.T.H. Chang, P. Knight, A.J.B. Vincent, Microstructural development in equiatomic multicomponent alloys, Materials Science and Engineering: A. 375–377 (2004) 213–218. https://doi.org/10.1016/j.msea.2003.10.257.

[3] J.W. Yeh, S.K. Chen, S.J. Lin, J.Y. Gan, T.S. Chin, T.T. Shun, C.H. Tsau, S.Y. Chang, Nanostructured high-entropy alloys with multiple principal elements: Novel alloy design concepts and outcomes, Adv Eng Mater. 6 (2004) 299–303. https://doi.org/10.1002/adem.200300567.

[4] E. Lewin, Multi-component and high-entropy nitride coatings—A promising field in need of a novel approach, J Appl Phys. 127 (2020) 160901. https://doi.org/10.1063/1.5144154.

[5] E., J. Mahan, Physical Vapor Deposition of Thin Films, John Wiley & Sons, 2000.

[6] MarketCap, The Noble Gases, Https://Marketcap.Com.Au/the-Noble-Gases/. (2022).

[7] R. Daniel, J. Musil, Novel nanocomposite coatings : advances and industrial applications, Jenny Stanford Publishing, 2014.

[8] P.M. Martin, Handbook of Deposition Technologies for Films and Coatings, Elsevier, 2010.

[9] J.T. Gudmundsson, D. Lundin, Introduction to magnetron sputtering, in: High Power Impulse Magnetron Sputtering: Fundamentals, Technologies, Challenges and Applications, Elsevier, 2019: pp. 1–48. https://doi.org/10.1016/B978-0-12-812454-3.00006-1.

[10] P.J. Kelly, R.D. Arnell, Magnetron sputtering: a review of recent developments and applications, Vacuum. 56 (2000) 159–172. https://doi.org/10.1016/S0042-207X(99)00189-X.

[11] K. Sarakinos, J. Alami, S. Konstantinidis, High power pulsed magnetron sputtering: A review on scientific and engineering state of the art, Surf Coat Technol. 204 (2010) 1661–1684. https://doi.org/10.1016/j.surfcoat.2009.11.013.

[12] N. Brenning, J.T. Gudmundsson, M.A. Raadu, T.J. Petty, T. Minea, D. Lundin, A unified treatment of self-sputtering, process gas recycling, and runaway for high power impulse sputtering magnetrons, Plasma Sources Sci Technol. 26 (2017). https://doi.org/10.1088/1361-6595/aa959b.

[13] D. Lundin, A. Hecimovic, T. Minea, A. Anders, N. Brenning, J.T. Gudmundsson, Physics of high power impulse magnetron sputtering discharges, in: High Power Impulse Magnetron Sputtering: Fundamentals, Technologies, Challenges and Applications, Elsevier, 2019: pp. 265–332. https://doi.org/10.1016/B978-0-12-812454-3.00012-7.

[14] J.T. Gudmundsson, N. Brenning, D. Lundin, U. Helmersson, High power impulse magnetron sputtering discharge, Journal of Vacuum Science & Technology A: Vacuum, Surfaces, and Films. 30 (2012) 030801. https://doi.org/10.1116/1.3691832.

[15] H. Zhang, J.S. Cherng, Q. Chen, Recent progress on high power impulse magnetron sputtering (HiPIMS): The challenges and applications in fabricating VO2 thin film, AIP Adv. 9 (2019). https://doi.org/10.1063/1.5084031.

[16] D. Depla, S. Mahieu, Reactive Sputter Deposition, Springer, 2008.

[17] J. James, L. Enlow, L.R. Enlow, Thin Film Processes, in: J.J. Licari, L.R. Enlow (Eds.), Hybrid Microcircuit Technology Handbook, Elsevier, Westwood, NJ, 1998: pp. 63–103. https://doi.org/10.1016/B978-081551423-7.50005-5.

[18] T. Kubart, J.T. Gudmundsson, D. Lundin, Reactive high power impulse magnetron sputtering, in: High Power Impulse Magnetron Sputtering: Fundamentals, Technologies, Challenges and Applications, Elsevier, 2019: pp. 223–263. https://doi.org/10.1016/B978-0-12-812454-3.00011-5.

[19] W.D. Sproul, High-rate reactive DC magnetron sputtering of oxide and nitride superlattice coatings, Vacuum. 51 (1998) 641–646. https://doi.org/https://doi.org/10.1016/S0042-207X(98)00265-6.

[20] K. Sarakinos, L. Martinu, Synthesis of thin films and coatings by high power impulse magnetron sputtering, in: High Power Impulse Magnetron Sputtering: Fundamentals, Technologies, Challenges and Applications, Elsevier, 2019: pp. 333–374. https://doi.org/10.1016/B978-0-12-812454-3.00013-9.

[21] S.O. Mbam, S.E. Nwonu, O.A. Orelaja, U.S. Nwigwe, X.F. Gou, Thin-film coating; Historical evolution, conventional deposition technologies, stress-state micro/nano-

level measurement/models and prospects projection: A critical review, Mater Res Express. 6 (2019). https://doi.org/10.1088/2053-1591/ab52cd.

[22] K. Seshan, D. Schepis, Handbook of Thin Film Deposition, Elsevier, 2018. https://doi.org/10.1016/C2016-0-03243-6.

[23] E. Alfonso, J. Olaya, G. Cubillos, Thin Film Growth Through Sputtering Technique and Its Applications, in: Crystallization - Science and Technology, InTech, 2012. https://doi.org/10.5772/35844.

[24] B. Movchan, A. V Demchishin, Study of the structure and properties of thick vacuum condensates of nickel, titanium, tungsten, aluminium oxide and zirconium dioxide, Phys. Met. Metallogr. (USSR). 28 (1969) 83–90.

[25] J.A. Thornton, High Rate Thick Film Growth, Annual Review of Materials Science. 7 (1977) 239–260. https://doi.org/10.1146/annurev.ms.07.080177.001323.

[26] R. Messier, A.P. Giri, R.A. Roy, Revised structure zone model for thin film physical structure, Journal of Vacuum Science & Technology A: Vacuum, Surfaces, and Films. 2 (1984) 500–503. https://doi.org/10.1116/1.572604.

[27] A. Anders, A structure zone diagram including plasma-based deposition and ion etching, Thin Solid Films. 518 (2010) 4087–4090. https://doi.org/10.1016/j.tsf.2009.10.145.

[28] O.N. Senkov, G.B. Wilks, D.B. Miracle, C.P. Chuang, P.K. Liaw, Refractory high-entropy alloys, Intermetallics (Barking). 18 (2010) 1758–1765. https://doi.org/10.1016/j.intermet.2010.05.014.

[29] J.W. Yeh, S.K. Chen, S.J. Lin, J.Y. Gan, T.S. Chin, T.T. Shun, C.H. Tsau, S.Y. Chang, Nanostructured high-entropy alloys with multiple principal elements: Novel alloy design concepts and outcomes, Adv Eng Mater. 6 (2004) 299–303. https://doi.org/10.1002/adem.200300567.

[30] D.R. Gaskell, D.E. Laughlin, Introduction to the Thermodynamics of Materials, CRC Press, 2017. https://doi.org/10.1201/9781315119038.

[31] J.-W. Yeh, Recent progress in high-entropy alloys, Annales de Chimie Science Des Matériaux. 31 (2006) 633–648. https://doi.org/10.3166/acsm.31.633-648.

[32] J. Dąbrowa, M. Zajusz, W. Kucza, G. Cieślak, K. Berent, T. Czeppe, T. Kulik, M. Danielewski, Demystifying the sluggish diffusion effect in high entropy alloys, J Alloys Compd. 783 (2019) 193–207. https://doi.org/10.1016/j.jallcom.2018.12.300.

[33] J.W. Yeh, Alloy design strategies and future trends in high-entropy alloys, JOM. 65 (2013) 1759–1771. https://doi.org/10.1007/s11837-013-0761-6.

[34] O.N. Senkov, D.B. Miracle, K.J. Chaput, J.P. Couzinie, Development and exploration of refractory high entropy alloys - A review, J Mater Res. 33 (2018) 3092–3128. https://doi.org/10.1557/jmr.2018.153.

[35] Z.D. Han, H.W. Luan, X. Liu, N. Chen, X.Y. Li, Y. Shao, K.F. Yao, Microstructures and mechanical properties of TixNbMoTaW refractory high-entropy alloys, Materials Science and Engineering A. 712 (2018) 380–385. https://doi.org/10.1016/j.msea.2017.12.004.

[36] M.A. Tunes, V.M. Vishnyakov, Microstructural origins of the high mechanical damage tolerance of NbTaMoW refractory high-entropy alloy thin films, Mater Des. 170 (2019). https://doi.org/10.1016/j.matdes.2019.107692.

[37] X. Feng, J. Utama Surjadi, Y. Lu, Annealing-induced abnormal hardening in nanocrystalline NbMoTaW high-entropy alloy thin films, Mater Lett. 275 (2020) 128097. https://doi.org/10.1016/j.matlet.2020.128097.

[38] A. Xia, R. Franz, Thermal Stability of MoNbTaVW High Entropy Alloy Thin Films, Coatings. 10 (2020) 941. https://doi.org/10.3390/coatings10100941.

[39] A. Xia, A. Togni, S. Hirn, G. Bolelli, L. Lusvarghi, R. Franz, Angular-dependent deposition of MoNbTaVW HEA thin films by three different physical vapor deposition methods, Surf Coat Technol. 385 (2020). https://doi.org/10.1016/j.surfcoat.2020.125356.

[40] L. Bi, X. Li, Y. Hu, J. Zhang, X. Wang, X. Cai, T. Shen, R. Liu, Q. Wang, C. Dong, P.K. Liaw, Weak enthalpy-interaction-element-modulated NbMoTaW high-entropy alloy thin films, Appl Surf Sci. 565 (2021) 150462. https://doi.org/10.1016/j.apsusc.2021.150462.

[41] Y.-Y. Chen, S.-B. Hung, C.-J. Wang, W.-C. Wei, J.-W. Lee, High temperature electrical properties and oxidation resistance of V-Nb-Mo-Ta-W high entropy alloy thin films, Surf Coat Technol. 375 (2019) 854–863. https://doi.org/10.1016/j.surfcoat.2019.07.080.

[42] G.C. Gruber, M. Kirchmair, S. Wurster, M.J. Cordill, R. Franz, A new design rule for high entropy alloy diffusion barriers in Cu metallization, J Alloys Compd. 953 (2023). https://doi.org/10.1016/j.jallcom.2023.170166.

[43] H. Li, N. Jiang, J. Li, J. Huang, J. Kong, D. Xiong, Hard and tough (NbTaMoW)Nx high entropy nitride films with sub-stoichiometric nitrogen, J Alloys Compd. 889 (2022). https://doi.org/10.1016/j.jallcom.2021.161713.

[44] L. Chen, W. Li, P. Liu, K. Zhang, F. Ma, X. Chen, H. Zhou, X. Liu, Microstructure and mechanical properties of (AlCrTiZrV)Nx high-entropy alloy nitride films by reactive magnetron sputtering, Vacuum. 181 (2020). https://doi.org/10.1016/j.vacuum.2020.109706.

[45] Y. Xu, G. Li, Y. Xia, Synthesis and characterization of super-hard AlCrTiVZr high-entropy alloy nitride films deposited by HiPIMS, Appl Surf Sci. 523 (2020). https://doi.org/10.1016/j.apsusc.2020.146529.

[46] A. Xia, R. Dedoncker, O. Glushko, M.J. Cordill, D. Depla, R. Franz, Influence of the nitrogen content on the structure and properties of MoNbTaVW high entropy alloy thin films, J Alloys Compd. 850 (2021). https://doi.org/10.1016/j.jallcom.2020.156740.

[47] D.-S. Chen, M.-K. Chen, S.-Y. Chang, Multiprincipal-Element AlCrTaTiZr-Nitride Nanocomposite Film of Extremely High Thermal Stability as Diffusion Barrier for Cu Metallization, ECS Trans. 19 (2009) 751–762. https://doi.org/10.1149/1.3122130.

[48] R. Li, M. Li, C. Jiang, B. Qiao, W. Zhang, J. Xu, Thermal stability of AlCrTaTiZrMo-nitride high entropy film as a diffusion barrier for Cu metallization, J Alloys Compd. 773 (2019) 482–489. https://doi.org/10.1016/j.jallcom.2018.09.283.

[49] S.-C. Liang, D.-C. Tsai, Z.-C. Chang, T.-N. Lin, M.-H. Shiao, F.-S. Shieu, Thermally Stable TiVCrZrHf Nitride Films as Diffusion Barriers in Copper Metallization, Electrochemical and Solid-State Letters. 15 (2012) H5. https://doi.org/10.1149/2.012201esl.

[50] L.B. Freund, S. Suresh, Thin Film Materials Stress, Defect Formation and Surface Evolution, Cambridge University Press, 2003.

[51] C. Saringer, M. Tkadletz, C. Mitterer, Restrictions of stress measurements using the curvature method by thermally induced plastic deformation of silicon substrates, Surf Coat Technol. 274 (2015) 68–75. https://doi.org/10.1016/j.surfcoat.2015.04.038.

[52] C. Saringer, M. Tkadletz, C. Mitterer, Restrictions of stress measurements using the curvature method by thermally induced plastic deformation of silicon substrates, Surf Coat Technol. 274 (2015) 68–75. https://doi.org/10.1016/j.surfcoat.2015.04.038.

[53] G.C.A.M. Janssen, M.M. Abdalla, F. van Keulen, B.R. Pujada, B. van Venrooy, Celebrating the 100th anniversary of the Stoney equation for film stress: Developments from polycrystalline steel strips to single crystal silicon wafers, Thin Solid Films. 517 (2009) 1858–1867. https://doi.org/10.1016/j.tsf.2008.07.014.

[54] G.G. Stoney, The tension of metallic films deposited by electrolysis, Proceedings of the Royal Society of London. Series A, Containing Papers of a Mathematical and Physical Character. 82 (1909) 172–175. https://doi.org/10.1098/rspa.1909.0021.

[55] T. Islam, J. Zechner, M. Bernardoni, M. Nelhiebel, R. Pippan, A novel setup for wafer curvature measurement at very high heating rates, Review of Scientific Instruments. 88 (2017). https://doi.org/10.1063/1.4975378.

[56] P.A. Flinn, Principles and Applications of Wafer Curvature Techniques for Stress Measurements in Thin Films, Stanford, 1988.

[57] C.O.W. Trost, Thermo-mechanical behaviour of Mo-Ag thin films, University of Leoben, 2018.

[58] Four Point Probes by Bridge Technology, http://four-point-probes.com/finite-size-corrections-for-4-point-probe-measurements, (2022).

[59] A. Togni, Angular-dependent deposition of MoNbTaVW HEA thin films by DCMS, HiPIMS and CAD, Università degli Studi di Modena e Reggio Emilia, 2019.

[60] G.C. Gruber, A. Lassnig, S. Zak, C. Gammer, M.J. Cordill, R. Franz, Synthesis and structure of refractory high entropy alloy thin films based on the MoNbTaW system, Surf Coat Technol. 439 (2022). https://doi.org/10.1016/j.surfcoat.2022.128446.

[61] R.J. Gambino, P.E. Seiden, Correlation of the Superconducting Transition Temperature with an Empirical Pseudopotential Determined from Atomic Spectra, Phys Rev B. 2 (1970) 3571–3577. https://doi.org/10.1103/PhysRevB.2.3571.

[62] K. Danisman, S. Danisman, S. Savas, I. Dalkiran, Modelling of the hysteresis effect of target voltage in reactive magnetron sputtering process by using neural networks, Surf Coat Technol. 204 (2009) 610–614. https://doi.org/10.1016/j.surfcoat.2009.08.048.

[63] V. Petrman, J. Houska, Trends in formation energies and elastic moduli of ternary and quaternary transition metal nitrides, J Mater Sci. 48 (2013) 7642–7651. https://doi.org/10.1007/s10853-013-7582-4.

[64] E. Mohimi, B.B. Trinh, S. Babar, G.S. Girolami, J.R. Abelson, Chemical vapor deposition of Mn x N y films from bis(2,2,6,6-tetramethylpiperidido)manganese(II) and ammonia , Journal of Vacuum Science & Technology A: Vacuum, Surfaces, and Films. 34 (2016) 060603. https://doi.org/10.1116/1.4964839.

[65] A. Lippitz, T. Hübert, XPS investigations of chromium nitride thin films, Surf Coat Technol. 200 (2005) 250–253. https://doi.org/10.1016/j.surfcoat.2005.02.091.

[66] L. Vegard, Die Konstitution der Mischkristalle und die Raumfüllung der Atome, Zeitschrift Für Physik. 5 (1921) 17–26. https://doi.org/10.1007/BF01349680.

[67] C. Suryanarayana, M.G. Norton, X-Ray Diffraction, Springer US, Boston, MA, 1998. https://doi.org/10.1007/978-1-4899-0148-4.

[68] International Centre for Diffraction Data, Card no. 01-077-3482, Ti, n.d.

[69] International Centre for Diffraction Data, Card no. 00-035-0789, Nb, n.d.

[70] International Centre for Diffraction Data, Card no. 00-042-1120, Mo, n.d.

[71] International Centre for Diffraction Data, Card no. 00-038-1478, Hf, n.d.

[72] International Centre for Diffraction Data, Card no. 00-004-0788, Ta, n.d.

[73] International Centre for Diffraction Data, Card no. 00-004-0806, W, n.d.

[74] International Centre for Diffraction Data, Card no. 01-087-0631, TiN, n.d.

[75] International Centre for Diffraction Data, Card no. 00-035-0768, VN, n.d.

[76] International Centre for Diffraction Data, Card no. 03-065-2899, CrN, n.d.

[77] International Centre for Diffraction Data, Card no. 01-083-8037, MnN, n.d.

[78] International Centre for Diffraction Data, Card no. 00-035-0753, ZrN, n.d.

[79] International Centre for Diffraction Data, Card no. 03-065-0436, NbN, n.d.

[80] International Centre for Diffraction Data, Card no. 01-076-6656, MoN, n.d.

[81] International Centre for Diffraction Data, Card no. 01-070-2824, HfN, n.d.

[82] International Centre for Diffraction Data, Card no. 00-049-1283, TaN, n.d.

[83] International Centre for Diffraction Data, Card no. 01-079-5765, WN, n.d.

[84] G. Gottstein, Materialwissenschaft und Werkstofftechnik, Springer Berlin Heidelberg, Berlin, Heidelberg, 2014. https://doi.org/10.1007/978-3-642-36603-1.

[85] N.W. Ashcroft, N.D. Mermin, Solid State Physics, Holt, Rinehart and Winston, 1976.

[86] R. Daniel, K.J. Martinschitz, J. Keckes, C. Mitterer, The origin of stresses in magnetron-sputtered thin films with zone T structures, Acta Mater. 58 (2010) 2621–2633. https://doi.org/10.1016/j.actamat.2009.12.048.

[87] H. Oettel, R. Wiedemann, Residual stresses in PVD hard coatings, Surf Coat Technol. 76–77 (1995) 265–273. https://doi.org/10.1016/0257-8972(95)02581-2.

[88] G.C. Gruber, A. Lassnig, S. Zak, C. Gammer, M.J. Cordill, R. Franz, Thermal stability of MoNbTaTiW, MoNbTaVW and CrMoNbTaW thin films deposited by high power impulse magnetron sputtering, Surf Coat Technol. 454 (2023). https://doi.org/10.1016/j.surfcoat.2022.129189.

7. Appendix

HiPMS Discharge

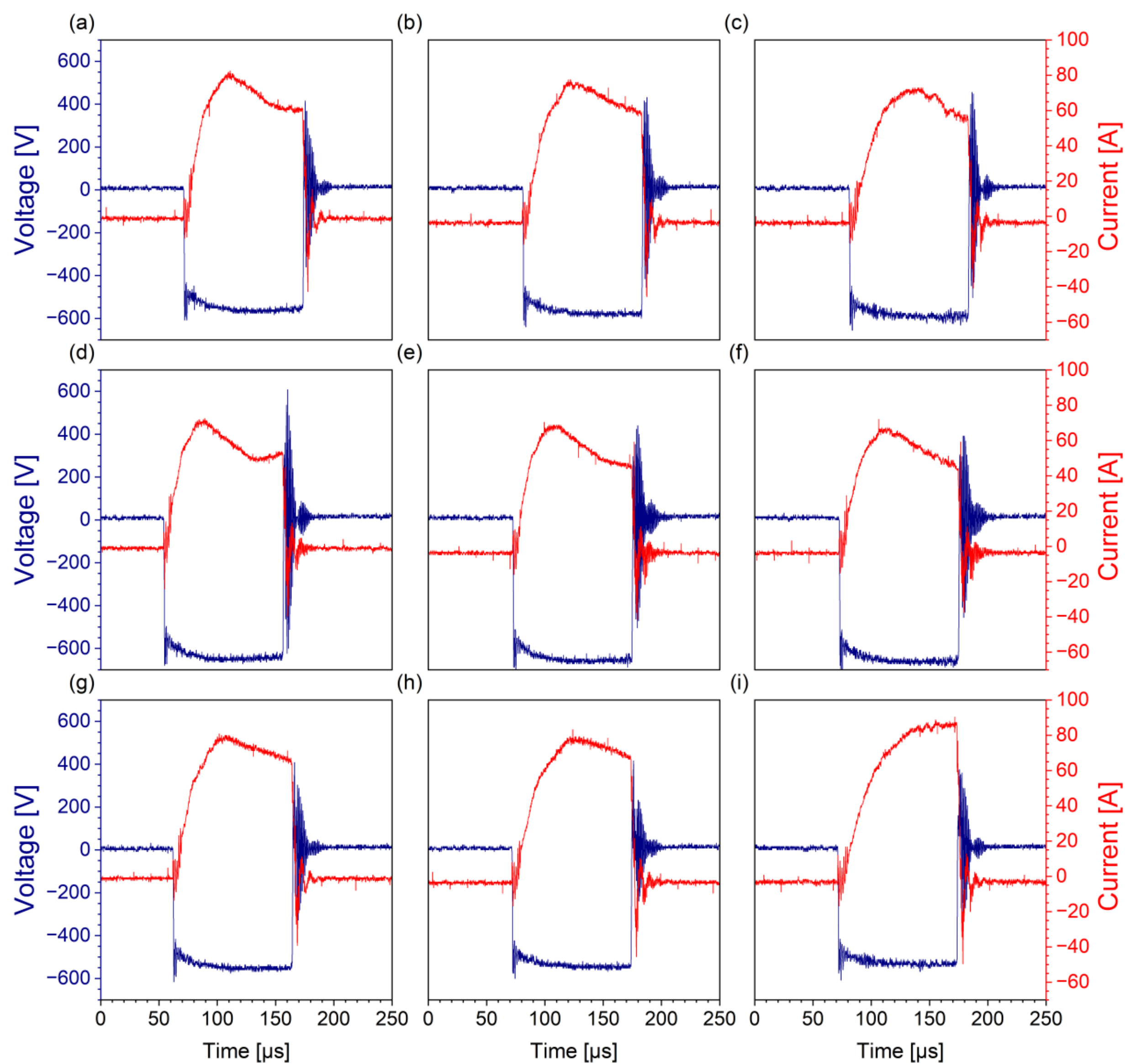

Figure 7-1: Voltage and current characteristics of the HiPIMS pulse of: MoNbTaVW (a) p(N_2) = 0.00 Pa, (b) p(N_2) = 0.09 Pa, (c) p(N_2) = 0.36 Pa; MnMoNbTaW (d) p(N_2) = 0.00 Pa, (e) p(N_2) = 0.09 Pa, (f) p(N_2) = 0.36 Pa and HfMoNbTaW (g) p(N_2) = 0.00 Pa, (h) p(N_2) = 0.09 Pa, (i) p(N_2) = 0.36 Pa.

Microstructure after annealing

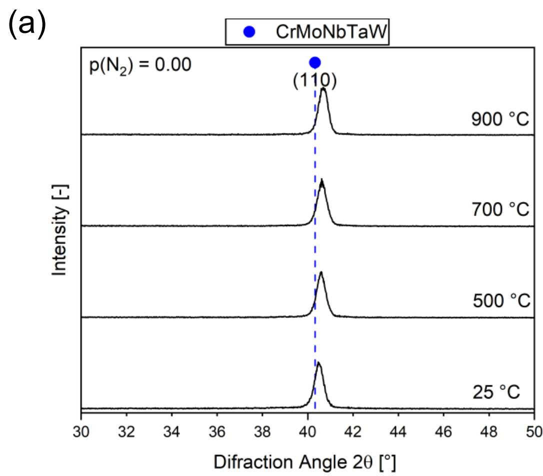

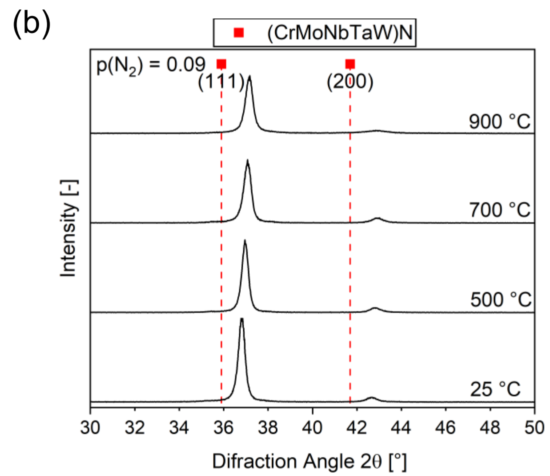

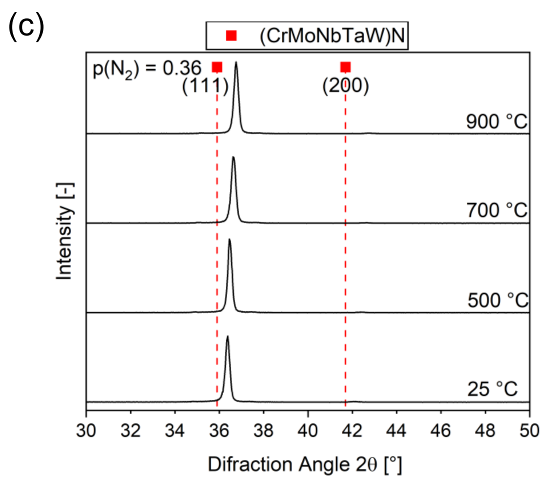

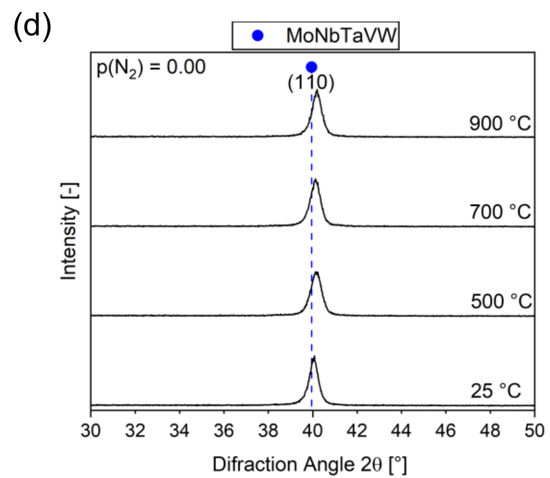

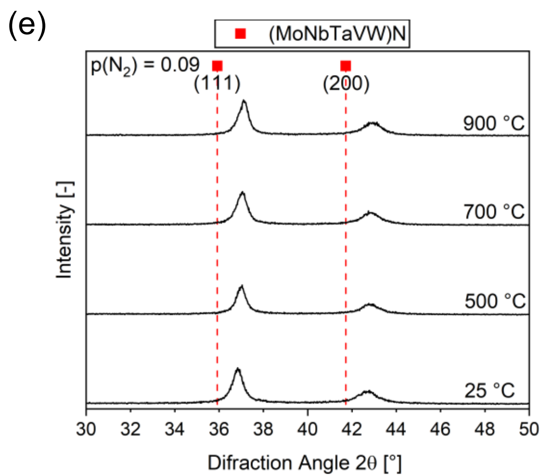

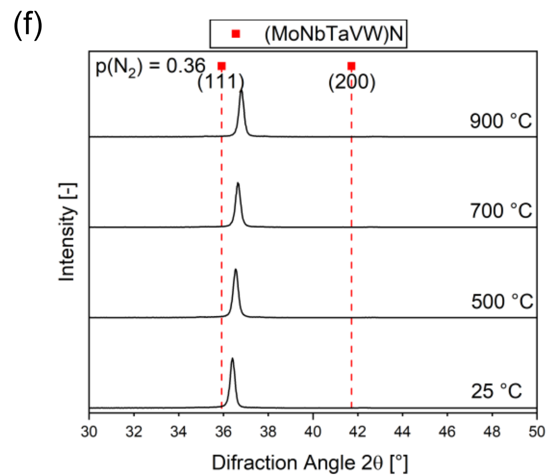

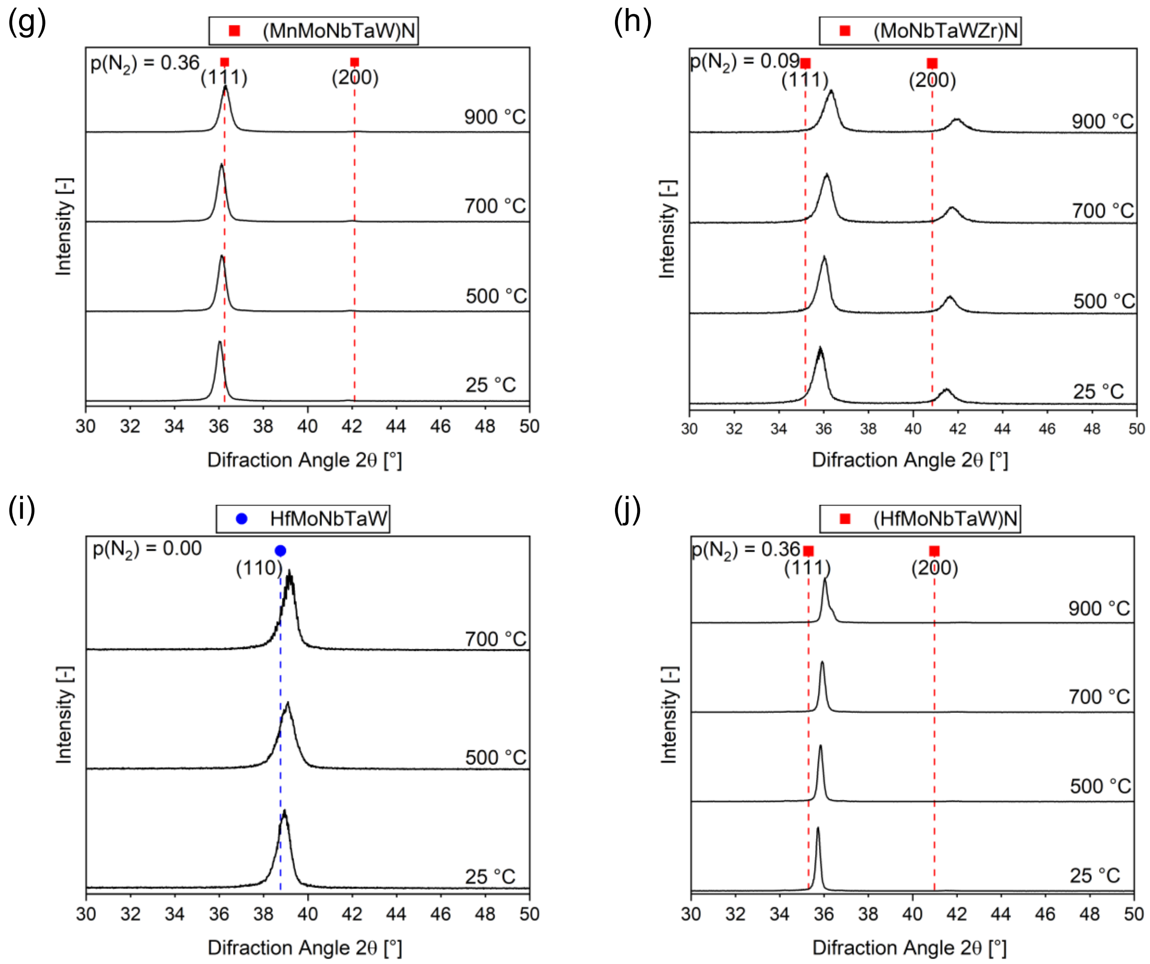

Figure 7-2: X-ray diffractograms after annealing of MnMoNbTaTiW at (a) $p(N_2)$ = 0.00 Pa, (b) $p(N_2)$ = 0.09 Pa, (c) $p(N_2)$ = 0.36 Pa, MoNbTaVW at (d) $p(N_2)$ = 0.00 Pa, (e) $p(N_2)$ = 0.09 Pa, (f) $p(N_2)$ = 0.36 Pa, MnMoNbTaW at (g) $p(N_2)$ = 0.36 Pa, MoNbTaWZr at (h) $p(N_2)$ = 0.36 Pa and HfMoNbTaW at (i) $p(N_2)$ = 0.00 Pa, (j) $p(N_2)$ = 0.36 Pa.

In-situ Stress Measurements

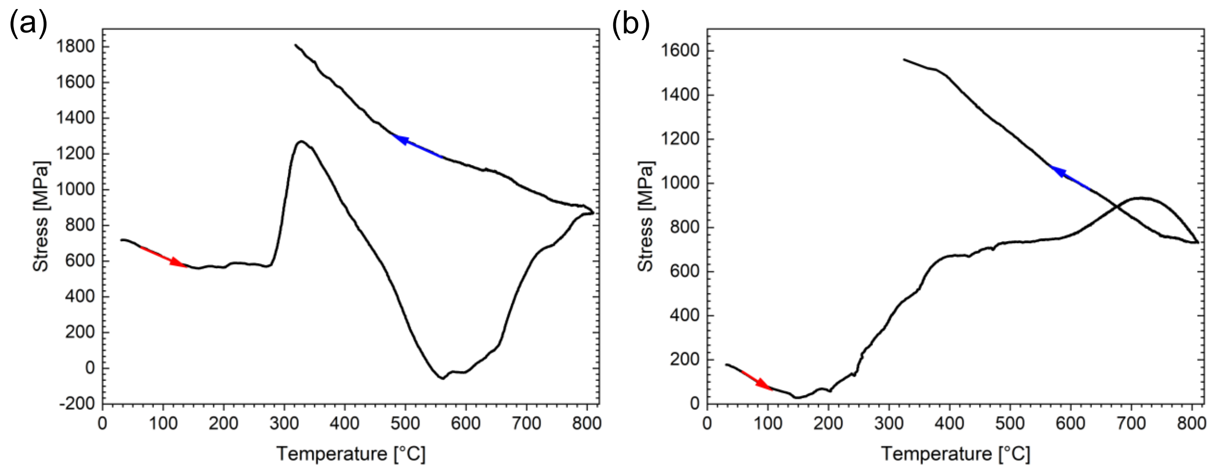

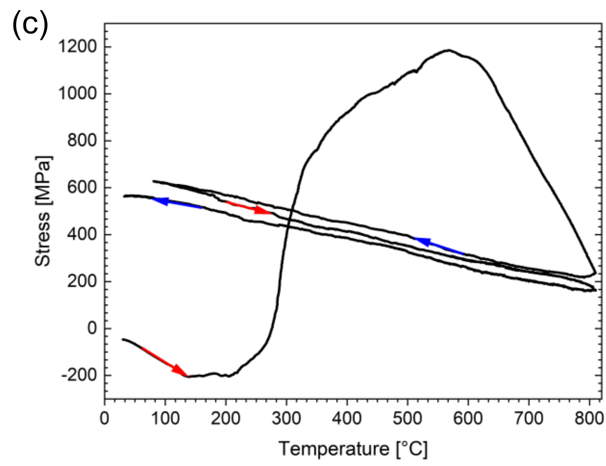

Figure 7-3: Stress-temperature curve of MoNbTaTiW at (a) $p(N_2)$ = 0.00 Pa, (b) $p(N_2)$ = 0.09 Pa and (c) $p(N_2)$ = 0.36 Pa.

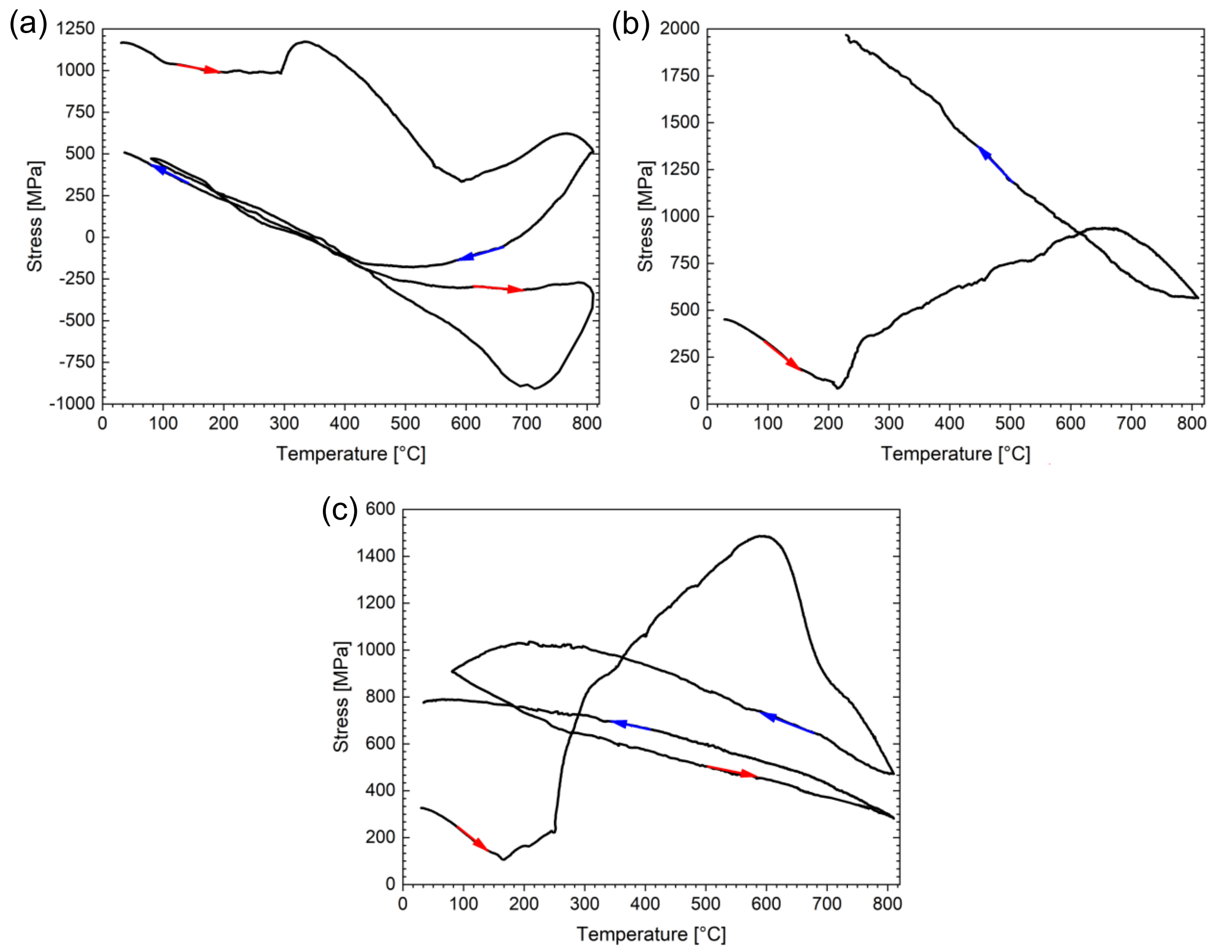

Figure 7-4: Stress-temperature curve of MoNbTaVW at (a) $p(N_2)$ = 0.00 Pa, (b) $p(N_2)$ = 0.09 Pa and (c) $p(N_2)$ = 0.36 Pa.

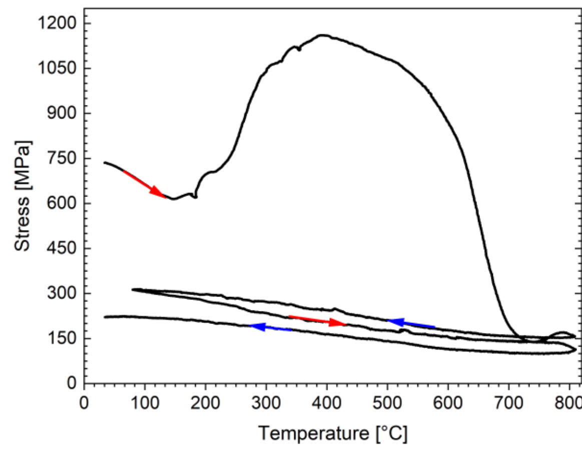

Figure 7-5: Stress-temperature curve of MnMoNbTaW at $p(N_2)$ = 0.00 Pa

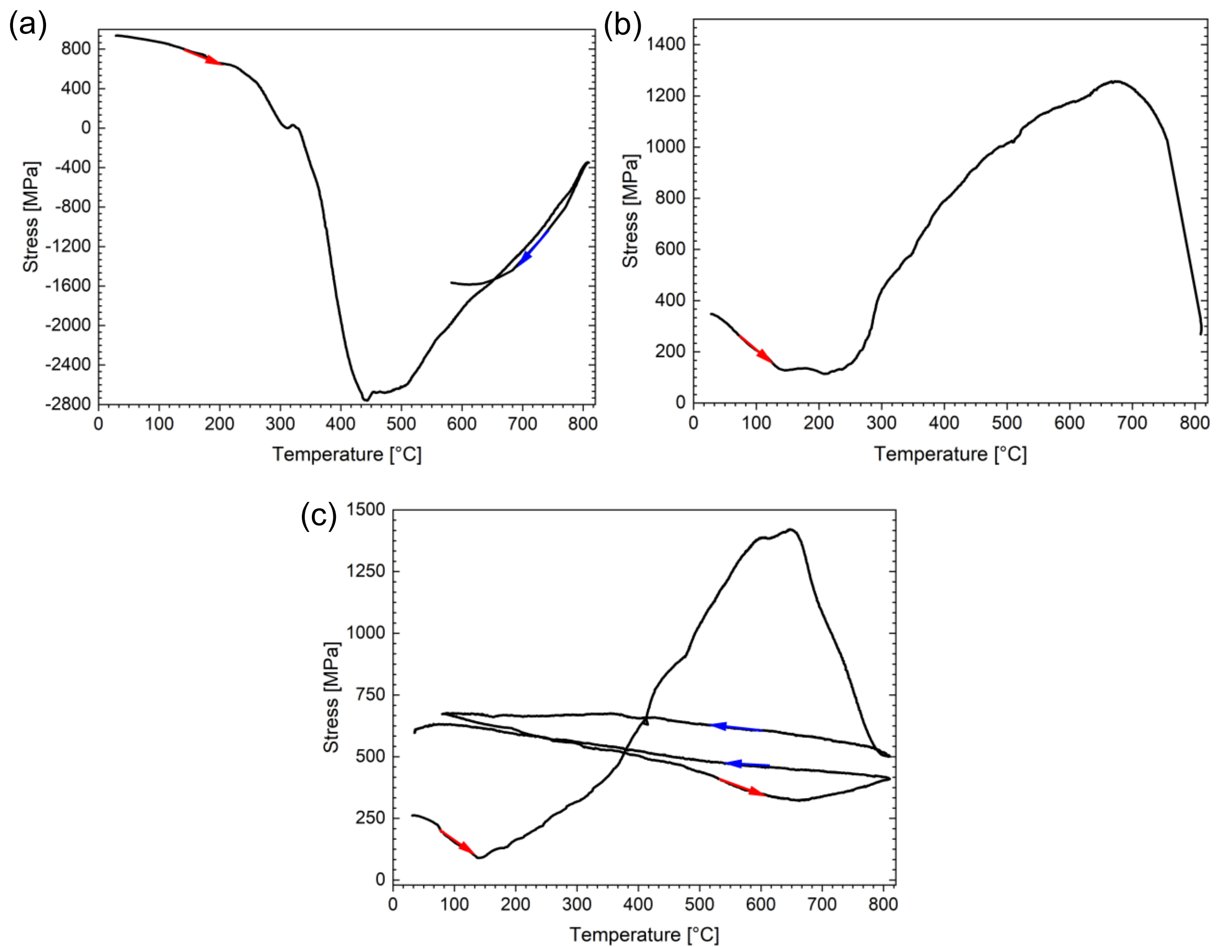

Figure 7-6: Stress-temperature curve of MoNbTaWZr at (a) $p(N_2)$ = 0.00 Pa, (b) $p(N_2)$ = 0.09 Pa and (c) $p(N_2)$ = 0.36 Pa.

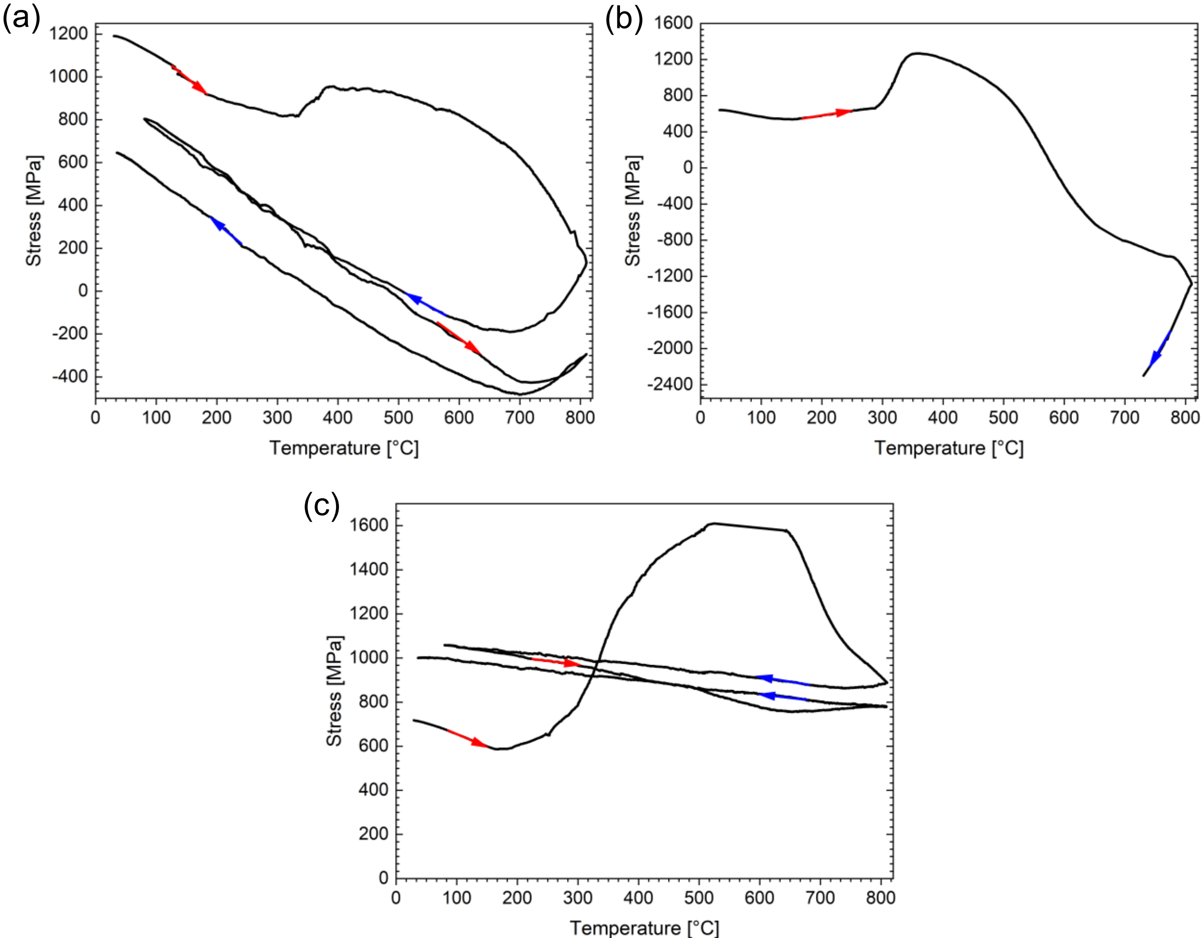

Figure 7-7: Stress-temperature curve of HfMoNbTaW at (a) $p(N_2)$ = 0.00 Pa, (b) $p(N_2)$ = 0.09 Pa and (c) $p(N_2)$ = 0.36 Pa.